8-2016

Study of Plasmonic Properties of the Gold Nanorods in the Visible to Near Infrared Light Regime

Pijush Kanti Ghosh
University of Arkansas, Fayetteville

Study of Plasmonic Properties of the Gold Nanorods in the Visible to Near Infrared Light Regime.

A thesis submitted in partial fulfillment
of the requirements for the degree of
Master of Science in Physics

by

Pijush Kanti Ghosh
University of Dhaka, Bangladesh
Master of Science in Physics, 2011
University of Dhaka, Bangladesh
Bachelor of Science in Physics, 2009

August 2016
University of Arkansas

This thesis is approved for recommendation to the Graduate Council.

Dr. Joseph B. Herzog
Thesis Director

Dr. Daniel Kennefick
Committee Member

Dr. Pradeep Kumar
Committee Member

Abstract

Nanostructures of noble metals show unique plasmonic behavior in the visible to near-infrared light range. Gold nanostructures exhibit a particularly strong plasmonic response for these wavelengths of light. In this study we have investigated optical enhancement and absorption of gold nanorods with different thickness using finite element method simulations. This study reports on the resonance wavelength of the sharp-corner and round-corner rectangles of constant length 100 nm and width 60 nm. The result shows that resonance wavelength depends on the polarization of the incident light; there also exists a strong dependence of the optical enhancement and absorption on the thickness of gold nanorods.

Acknowledgements

First I would like to show my gratitude to my principle advisor, Dr. Joseph B. Herzog, for providing me the chance to work in his Plasmonic Nano-optics group at the University of Arkansas, Fayetteville, USA. Without his support and cooperation, it would not be possible for me to reach the zenith of my research goal. He is a great advisor as well as a great teacher. I always like to follow his instructions about my research.

I would like to thank Dr. Daniel Kennefick and Dr. Pradeep Kumar for being respected thesis committee members. I appreciate them for their time and advice that has helped me very much to pursue my research goal.

I feel very blessed that, I am working in such a nice group where everyone is so helpful. I have learned a lot from them. They are very nice researchers as well as nice friends. Especially I would like to thank Desalegn T. Debu, Stephen J. Bauman, David A. French, Ahmad Darweesh and Saeed Sarollahi for their constructive comments and collaborative efforts on research and publications that have helped me to go in the right direction of my research.

I would like to thank my wife for her continuous support in every aspect of my life. I want to show my gratitude to my father-in-law and mother-in law for their inspirational support to study aboard. I am always thankful to my family back in Bangladesh who provide me full mental support to be a good researcher as well as a good person. I would like to thank my parents, sisters and brothers-in-law and my well-wishers for their belief in me, without them I am nothing. I want to thank Sonjoy K. Paul for his continuous support to pursue my aim in life.

Finally, I want to express my gratitude to the Department of Physics, the Fulbright College of Arts and Sciences and the Graduate School for giving me the opportunity to study here at the

University of Arkansas, Fayetteville, USA. Without their support it would not be possible for me to pursue my dream.

Dedication

This thesis is dedicated to my Father, Mother, Father-in-law, Mother-in-law, Wife, Sisters, Brothers-in-law, Sonjoy and my friends. Thank you so much.

Table of Contents

List of figures

1 Chapter: INTRODUCTION

1.1 Motivation

The conduction electrons of metal nanoparticles oscillate collectively when incident light illuminates the metal nanoparticles. This collective oscillation is known as a *surface plasmon* or simply just a *plasmon*. Local-field enhancements, light absorption and scattering occur at the resonant wavelength because of the large optical polarization [1]–[3]. Due to their small volume, gold nanorods exhibit little radiation damping as a result they show large local-field enhancement factors and large light scattering efficiency. Because of these characteristics nanorods prove interesting for optical applications [1].

Nanorods can be used as nanoantennae. Nanoantenne have been shown useful for many applications such as in enhancing light-emitter interactions [4]–[6], high-resolution microscopy and spectroscopy [7], optical sensors [8]–[11], plasmonics in THz range [12], solar cells [13]–[19], etc.

Saylor et al. studied optical enhancement of gold nanowires and triple nanowire arrays using a two dimensional finite element method and they observed that increasing the width of the nanowire redshifted the resonance wavelengths [20]. Qiu et al. observed the plasmon resonance and saturable absorption of gold nanorods [21]. Jain et al. studied colloidal gold nanorods in different refractive index; they also studied plasmon coupling between gold nanodiscs. They found that the near-field coupling strength between two nanodiscs [22]. Plasmonic properties of metal nanostructures depend on their size, shape and dielectric environment. For the triangular silver prism, extinction spectra have been studied and multimode resonances have been found [23]. The light scattering from nanocuboid and rectangular cuboidal nanoantennae are calculated

by an analytical approach [24]. Using a quasistatic approximation, plasmon energy distribution, linewidth, resonant frequency of the nanostructures, and the effect of the optical gain were driven by Wang et al. [25]. Nanostructures can be made in many different ways; Shao et al. have shown that chemically grown nanostructures show larger scattering amplitudes than nanostructures created via electron beam lithography [26]. Langhammer et al. have studied Pt, Pd, Ag, and Au nanodiscs made by a hole-mask colloidal lithography process, and they observed that increasing the radius of the discs blue shifted, the scattering, absorption and extinction efficiency spectra shifts toward blue [27].

Aluminum is also a promising candidate in plasmonic research because of its low cost and availability. It also shows versatile optical properties on optical frequencies. Knight et al studied Al nanostructures and they have calculated scattering spectra for normal incidence; they found that with increasing length of the nanoantenna, the resonant wavelength decreases toward the ultraviolet light regime [28], [29]. Extinction spectra were observed in Al nanospheres made by extreme ultraviolet lithography; increasing the diameter of the nanoparticles caused the plasmon resonance to shift toward red. For the same size of the nanoparticles of different metals such as gold, aluminum and silver show different peak resonances [30]. Lecarme et al. fabricated Al nanorods using electron beam lithography and observed absorption at near-infrared wavelengths [31].

Giannini et al. fabricated gold nanoparticles of different shapes using electron beam lithography, and they have experimentally shown the scattering intensity and the resonance wavelengths of the nanoparticles. They have also calculated the depolarization factor as a function of cuboid length and ellipsoid length [32]. Zhang et al. studied substrate-induced Fano resonances of Ag nanocubes and found a strong substrate effect on localized surface plasmon

resonances [10]. Muskens et al. measured the scattering spectra of gold nanorods of various lengths, and they found, that increasing the length of the nanorods shifted the resonance wavelengths toward blue [33]. Polarization dependent plasmonic resonance was by Huang et al. using dark field microscopy, and they found that resonant modes strongly depend on the incident light polarization [34]. They also found multiple plasmon modes and near-field enhancement using surface-enhanced Raman scattering in closely spaced gold nanorod arrays [35].

The full width half maxima (FWHM) of the absorption band of gold nanorods fabricated chemically were studied as a function of aspect ratio. The Drude model and quasi-static model were used to calculate FWHM, and it was found that the longitudinal absorption peak is wider than that of the transverse mode. It was also found, that increasing the aspect ratio nonlinearly increased the FWHM of longer wavelength absorption peaks [36]. Kooij et al. studied the influence of size and shape of randomly oriented nanorods on their optical properties using discrete dipole approximation (DDA). They observed that longitudinal plasmon resonance of the nanorods is affected by rod aspect ratio [37], [38]. Hill et al. investigated a computational electromagnetic analysis of GaAs photodetectors with gold interdigital electrodes and found photoresponse of the device depends largely on spacing between the electrodes and on the incident light polarization [39]. Abbey et al. studied the photocurrent generation and and the effect of the Ti adhesion layer used to adhere the gold nanostructures to the GaAs substrate [40]. Wu et al investigated angle-resolved plasmonic properties of single gold dimers [41].

1.2 Finite element method (FEM)

1.2.1 Principle of the finite element method:

Converting partial differential equations into linear algebraic equation sets in order to produce approximate solutions for the boundary-value problems is known as the finite element method [42], [43]. So far, two methods are being used to formulate the finite element method: the variational method and the weighted residual method. The weighted residual method starts working from the partial differential equation of the boundary-value problem. The variational method starts from the variational representation of the boundary-value problem. Here, weighted residual method is discussed.

Let us consider a partial differential equation

$$\mathfrak{T}\varphi = f \tag{1.1}$$

here, $\mathfrak{T}$ known as the differential operator and φ is the unknown solution, and f is called the source function. Now, φ is expressed as a set of basis functions.

$$\varphi = \sum_{j=1}^{N} c_j v_j \tag{1.2}$$

where, c_j represents the expansion coefficients corresponding to the basis functions v_j where j = *1, 2, 3… N.* Substituting equation (1.2) into equation (1.1) and then integrating over the entire solution domain Ω, with a weighted function w_i gives

$$\int w_i \mathfrak{T}\left(\sum_{j=1}^{N} c_j v_j\right) d\Omega = \int w_i f d\Omega \tag{1.3}$$

From equation (1.3), c_j can be determined by applying proper boundary conditions to the problem. By choosing $w_i = v_i$ and formulating it like Galerkin's method [44], equation (1.3) can be written as:

$$\sum_{j=1}^{N} c_j \int v_i \mathfrak{T}(v_j) d\Omega = \int v_i f d\Omega \tag{1.4}$$

here, *i=1, 2, 3, 4……..N*.

Let $S_{ij} = \int v_i \mathfrak{T}(v_j) d\Omega$ and $b_i = \int v_i f d\Omega$ then equation (1.4) can be written as:

$$\sum_{j=1}^{N} S_{ij} c_j = b_i \tag{1.5}$$

$S_{ij} = S_{ji}$ for a self-adjoint problem, and the coefficient matrix that can be obtained from equation (1.5) is symmetric. In that case

$$\int v_i \mathfrak{T}(v_j) d\Omega = \int v_j \mathfrak{T}(v_i) d\Omega \tag{1.6}$$

The difficult part of the finite element method is to find a set of basis functions. To simplify the solution determined by the finite element method, one first needs to divide the domain into small subdomains, which are known as finite elements; then uses a simple function to approximate the unknown solutions for each element. These functions could be linear or quadratic.

1.2.2 Finite element method for electrodynamics

Consider a domain with electric current density $\boldsymbol{J}$, which has permittivity ε and permeability μ. Due to this current density the electric field intensity $\boldsymbol{E}$ can be calculated by the Maxwell's equations.

$$\nabla \times \boldsymbol{E} = -j\omega\mu\boldsymbol{H} \tag{1.7}$$

$$\nabla \times \boldsymbol{H} = j\omega\tilde{\varepsilon}\boldsymbol{E} + \boldsymbol{J} \tag{1.8}$$

$$\nabla.(\tilde{\varepsilon}\boldsymbol{E}) = -\frac{1}{j\omega}\nabla.\boldsymbol{J} \tag{1.9}$$

$$\nabla.(\mu\boldsymbol{H}) = 0 \tag{1.10}$$

By eliminating $\boldsymbol{H}$ from equation (1.7) and (1.8), the equations can be combined as:

$$\nabla \times \left(\frac{1}{\mu_r}\nabla \times \boldsymbol{E}\right) - k_0^2\varepsilon_r\boldsymbol{E} = -jk_0Z_0\boldsymbol{J} \tag{1.11}$$

$$\nabla \times \left(\frac{1}{\mu_r}\nabla \times \boldsymbol{E}\right) - k_0^2\left(\varepsilon_r - \frac{j\sigma}{\omega\varepsilon_0}\right)\boldsymbol{E} = 0 \tag{1.12}$$

where $\mu_r = \frac{\mu}{\mu_0}$ is the relative permeability and $\varepsilon_r = \frac{\tilde{\varepsilon}}{\varepsilon_0}$ is called relative permittivity.

Also k_0 is called the free space wavenumber and $Z_0$is called the intrinsic impedance.

$$k_0 = \omega\sqrt{\mu_0\varepsilon_0} \tag{1.13}$$

$$Z_0 = \sqrt{\mu_0/\varepsilon_0} \tag{1.14}$$

Typically for a perfectly conducting surface, homogenous Dirichlet conditions are used, and mixed boundary conditions are used for the impedance surface. For these two conditions, the following are assumed.

$$\hat{n} \times \boldsymbol{E} = \boldsymbol{P} \qquad \text{on } \Gamma_D \tag{1.15}$$

$$\hat{n} \times \left(\frac{1}{\mu_r}\nabla \times \boldsymbol{E}\right) + \frac{jk_0}{\eta_r}\hat{n} \times (\hat{n} \times \boldsymbol{E}) = \boldsymbol{K}_N \quad \text{on } \Gamma_N \tag{1.16}$$

where **P** is the tangential value of the electric field on Γ_D, η_r is known as normalize surface impedance on Γ_N, and $\mathbf{K}_N$ is a known function representing a boundary source on Γ_N.

Now equation (1.11) is multiplied by an appropriate weighting function $\mathbf{W}_i$ and integrated over the problem domain.

$$\int \boldsymbol{W}_i . \left[\nabla \times \left(\frac{1}{\mu_r}\nabla \times E\right) - k_0^2 \varepsilon_r E\right] d\Omega = -jk_0 Z_0 \int \boldsymbol{W}_i . J d\Omega \tag{1.17}$$

By using the vector identity

$$\nabla . \left[\boldsymbol{W}_i \times \left(\frac{1}{\mu_r}\nabla \times \boldsymbol{E}\right)\right] = \frac{1}{\mu_r}(\nabla \times \boldsymbol{W}_i).(\nabla \times \boldsymbol{E}) - \boldsymbol{W}_i . \left[\nabla \times \left(\frac{1}{\mu_r}\nabla \times \boldsymbol{E}\right)\right] \tag{1.18}$$

and Gauss's theorem

$$\int \nabla . \left[\boldsymbol{W}_i \times \left(\frac{1}{\mu_r}\nabla \times \boldsymbol{E}\right)\right] d\Omega = \oint \hat{n} . \left[\boldsymbol{W}_i \times \left(\frac{1}{\mu_r}\nabla \times \boldsymbol{E}\right)\right] d\Gamma \tag{1.19}$$

we obtain the weak-form representation of equation (1.11) as

$$\begin{aligned} \int \left[\frac{1}{\mu_r}(\nabla \times \boldsymbol{W}_i).(\nabla \times \boldsymbol{E}) - k_0^2 \varepsilon_r \boldsymbol{W}_i . \boldsymbol{E}\right] d\Omega \\ = \int \frac{1}{\mu_r}(\hat{n} \times \boldsymbol{W}_i).(\nabla \times \boldsymbol{E}) d\Gamma \\ - \int \left[\frac{jk_0}{\eta_r}(\hat{n} \times \boldsymbol{W}_i).(\hat{n} \times \boldsymbol{E}) + \boldsymbol{W}_i . \boldsymbol{K}_N\right] d\Gamma \\ - jk_0 Z_0 \int \boldsymbol{W}_i . \boldsymbol{J} d\Omega \end{aligned} \tag{1.20}$$

after the boundary condition in equation (1.16) is applied.

To get the numerical solution of equation (1.20) using the finite element method, the entire domain Ω is divided up into small finite elements. For a 2-D domain, triangular elements and for 3-D domain tetrahedral elements need to be made. The method takes into account the tangential

components of the electric field at the edge of each element, and then interpolates **E** elsewhere using a vector basis function [42]. The electric field in a tetrahedral element is shown as

$$\begin{aligned} E^{(e)}(x,y,z) = {} & \boldsymbol{N}_{12}^{(e)}(x,y,z)E_{12}^{(e)} + \boldsymbol{N}_{13}^{(e)}(x,y,z)E_{13}^{(e)} + \boldsymbol{N}_{14}^{(e)}(x,y,z)E_{14}^{(e)} \\ & + \boldsymbol{N}_{23}^{(e)}(x,y,z)E_{23}^{(e)} + \boldsymbol{N}_{24}^{(e)}(x,y,z)E_{24}^{(e)} \\ & + \boldsymbol{N}_{34}^{(e)}(x,y,z)E_{34}^{(e)} \end{aligned} \tag{1.21}$$

where $E_{lk}^{(e)}$ is known as the tangential components of the electric field at the edge of the element *e* that connects the node *l* and *k*. Also the interpolation function is defined by $N_{lk}^{(e)}$, which is known as basis function. Now $N_{lk}^{(e)}$ can be defined as

$$\boldsymbol{N}_{lk}^{(e)}(\mathbf{r}) = \left[N_l^{(e)}\nabla N_k^{(e)} - N_k^{(e)}\nabla N_l^{(e)}\right] l_{lk}^{(e)} \qquad l < k$$

here, $N_l^{(e)}$ and $N_k^{(e)}$ are the linear scalar interpolation functions associated with nodes *l* and *k* of a tetrahedral element and $l_{lk}^{(e)}$is known as the signed length of the edge that connects the nodes *l* and *k*. Using interpolated tangential values of the electric field in each element, the total field **E** can be expressed as

$$\boldsymbol{E} = \sum_{j=1}^{N_{edge}} \boldsymbol{N}_j E_j + \sum_{j=1}^{N_D} \boldsymbol{N}_j^D E_j^D \tag{1.22}$$

here, N_{edge} is the total number of edges excluding those on Γ_D, E_j denotes the tangential component of **E** at the *j*th edge and $\mathbf{N}_j$ is the corresponding vector basis function and total number of edges denoted by $\boldsymbol{N}_D$. Also E_j^D and $\boldsymbol{N}_j^D$ are known as the tangential **E**- field and corresponding basis functions, respectively. $\boldsymbol{N}_j$ spans over nearer elements adjacent to edge *j*. Now equation (1.22) is plugged in the equation (1.20) and, we obtain

$$\sum_{j=1}^{N_{edge}} K_{ij}E_j = b_j \tag{1.23}$$

where

$$K_{ij} = \int \left[\frac{1}{\mu_r}(\nabla \times \boldsymbol{N}_i).(\nabla \times \boldsymbol{N}_j) - k_0^2 \varepsilon_r \boldsymbol{N}_i.\boldsymbol{N}_j\right] d\Omega + jk_0 \int \left[\frac{1}{\eta_r}(\hat{n} \times \boldsymbol{N}_i).(\hat{n} \times \boldsymbol{N}_j)\right] d\Gamma$$

and

$$b_i = -jk_0 Z_0 \int \boldsymbol{N}_i.\boldsymbol{J}\, d\Omega - \int \boldsymbol{N}_i.\boldsymbol{K}_N\, d\Gamma - \sum_{j=1}^{N_D} E_j^D \int \left[\frac{1}{\mu_r}(\nabla \times \boldsymbol{N}_i).(\nabla \times \boldsymbol{N}_j^D) - k_0^2 \varepsilon_r \boldsymbol{N}_i.\boldsymbol{N}_j^D\right] d\Omega$$

The integral over Γ_D in equation (1.20) vanishes because of $\hat{n} \times \boldsymbol{N}_i = 0$ on Γ_D. Then equation (1.23) can written as

$$[K]\{E\} = \{b\} \tag{1.24}$$

where $[K]$, denotes a sparse and symmetric matrix which can be solved by a sparse matrix solver. When {E} is found then the electric field can be obtained all over the domain by equation (1.22).

2 Chapter: BACKGROUND

2.1 Theoretical background

2.1.1 Electrodynamics in matter

In the low frequency regime, a small fraction of the electromagnetic waves penetrates matter when we consider the perfect or good conductor approximation. Field penetration increases in the metal at higher frequencies, i.e. near-infrared and visible light regions. In these regions, dissipation also occurs in the metal structures. In the ultraviolet frequencies metals obtain dielectric behavior, however in this region light waves can propagate through the metals. Noble metals such as gold, silver shows strong absorption at these wavelengths because of their interband transitions of the electrons. These dispersive properties of the metals can be described by the complex dielectric function $\varepsilon(\omega)$ [45]. Starting from the macroscopic electromagnetism of the Maxwell's equations:

$$\nabla . \boldsymbol{D} = \rho_{ext} \tag{2.1}$$

$$\nabla . \boldsymbol{B} = 0 \tag{2.2}$$

$$\nabla \times \boldsymbol{E} = -\frac{\partial \boldsymbol{B}}{\partial t} \tag{2.3}$$

$$\nabla \times \boldsymbol{H} = \boldsymbol{J}_{ext} + \frac{\partial \boldsymbol{D}}{\partial t} \tag{2.4}$$

These equations connect four macroscopic fields such as ***D, E, H*** and ***B***, with the external charge and current densities ρ_{ext} and $\boldsymbol{J_{ext}}$. Here, ***D*** represents dielectric displacement, ***E*** is the electric field, ***H*** is the magnetic field and ***B*** is the magnetic induction of magnetic flux density. ρ_{tot} and $\boldsymbol{J}_{tot}$ can be defined as:

$$\rho_{tot} = \rho_{ext} + \rho \tag{2.5}$$

$$\boldsymbol{J_{tot}} = \boldsymbol{J_{ext}} + \boldsymbol{J} \tag{2.6}$$

In equation (2.5) and (2.6) used ρ and $\boldsymbol{J}$ are known as internal charge and current densities. However, the external set (ρ_{ext},$\boldsymbol{J}_{ext}$) drives the system and internal the set (ρ, $\boldsymbol{J}$) responds to the external set.

Inside the metal, the fields are connected via polarization **P** and magnetization **M** by

$$\boldsymbol{D} = \varepsilon_0 \boldsymbol{E} + \boldsymbol{P} \tag{2.7}$$

$$\boldsymbol{H} = \frac{\boldsymbol{B}}{\mu_0} - \boldsymbol{M} \tag{2.8}$$

where, ε_0 is the electric permittivity of a vacuum and μ_0 is the magnetic permeability of a vacuum. Considering the nonmagnetic case, polarization, internal charge density, ρ is linked with polarization, $\boldsymbol{P}$ (defined as electric dipole moment per unit volume inside the metals) by:

$$\nabla . \boldsymbol{P} = -\rho \tag{2.9}$$

and charge conservation is defined by:

$$\nabla . \boldsymbol{J} = \frac{\partial \rho}{\partial t} \tag{2.10}$$

From equation (2.9) and (2.10), a relationship between $\boldsymbol{J}$ and $\boldsymbol{P}$ can be obtained.

$$\boldsymbol{J} = \frac{\partial \boldsymbol{P}}{\partial t} \tag{2.11}$$

By putting equation (2.7) in equation (2.1), the relationship between the electric field and total charge density is obtained

$$\nabla . \boldsymbol{E} = \frac{\rho_{tot}}{\varepsilon_0} \tag{2.12}$$

For a linear, isotropic and nonmagnetic medium, dielectric displacement ($\boldsymbol{D}$) and magnetic flux density (**B**) can be defined as:

$$\boldsymbol{D} = \varepsilon_r \varepsilon_0 \boldsymbol{E} \tag{2.13}$$

and

$$\boldsymbol{B} = \mu\mu_0\boldsymbol{H} \tag{2.14}$$

here, $\varepsilon_r(\omega) = \frac{\tilde{\varepsilon}(\omega)}{\varepsilon_0}$ [46], ε_r is known as dielectric constant also known as relative permittivity and μ is known as the relative permeability of the magnetic medium, ε_0 is the vacuum permittivity and $\tilde{\varepsilon}(\omega)$ is the complex frequency-dependent absolute permittivity of the material. However, there is a relationship between polarizations and the electric field described in [47].

$$\boldsymbol{P} = \varepsilon_0\chi\boldsymbol{E} \tag{2.15}$$

And

$$\varepsilon_r(\omega) = \frac{\tilde{\varepsilon}(\omega)}{\varepsilon_0} = 1 + \chi \tag{2.16}$$

here, χ is the electric susceptibility [46]. Also the current density has a relationship with the electric field [48], [46]:

$$\boldsymbol{J} = \sigma\boldsymbol{E} \tag{2.17}$$

These equations are true for the linear media where it does not show temporal or spatial dispersion. The optical response of metals depends on the frequency. It also depends on the wave vector. We can generalize the linear relationship by taking account of the non-locality in time and space.

$$\boldsymbol{D}(\boldsymbol{r}, t) = \varepsilon_0 \int dt' \boldsymbol{dr}' \varepsilon_r(\boldsymbol{r} - \boldsymbol{r}', t - t')\boldsymbol{E}(\boldsymbol{r}', t') \tag{2.18}$$

$$\boldsymbol{J}(\boldsymbol{r}, t) = \int dt' \boldsymbol{dr}' \sigma(\boldsymbol{r} - \boldsymbol{r}', t - t')\boldsymbol{E}(\boldsymbol{r}', t') \tag{2.19}$$

Applying the Fourier transformation we can decompose the fields into plane wave components as functions of $\boldsymbol{K}$ and angular frequency ω. Then we can get,

$$\boldsymbol{D}(\boldsymbol{K},\omega) = \varepsilon_0 \varepsilon_r(\boldsymbol{K},\omega)\boldsymbol{E}(K,\omega) \tag{2.20}$$

$$\boldsymbol{J}(\boldsymbol{K},\omega) = \sigma(\boldsymbol{K},\omega)\boldsymbol{E}(\boldsymbol{K},\omega) \tag{2.21}$$

Using these equations we get the final relationship between the dielectric constant and the conductivity.

$$\varepsilon_r(\boldsymbol{K},\omega) = 1 + \frac{i\sigma(\boldsymbol{K},\omega)}{\varepsilon_0 \omega} \tag{2.22}$$

When the light interacts with metals, the dielectric constant ε_r (ω, $\boldsymbol{K}$) can be simplified by ε_r (ω, $K=0$), it is assumed that the limit of a spatially local response. This simplification only works when the wavelength in the material is longer than the size of the unit cell or mean free path of the electrons. This simplification works well at ultraviolet frequencies [45].

At low frequencies, ε_r describes the response of the bound charges to the incident electric field and σ describes the contribution of free charges to the current flow. Dielectric function is a complex function and it can be obtained from the complex refractive index which is described in chapter 4. The real value of the refractive index can be defined as:

$$n^2 = \frac{\varepsilon_1}{2} + \frac{1}{2}\sqrt{\varepsilon_1^2 + \varepsilon_2^2} \tag{2.23}$$

where, ε_1 is knows as real part of the dielectric constant and ε_2 is known as the imaginary part of the dielectric function. The imaginary value of the refractive index can be defined as:

$$\kappa = \frac{\varepsilon_2}{2n} \tag{2.24}$$

here, κ is called the extinction coefficient. Optical absorption inside the medium due to the electromagnetic wave can be determined by the κ. The absorption coefficient (α) is defined by in Beer's law which describes the attenuation of beam intensity when it propagates through the medium ($I(x) = I_0 e^{-\alpha x}$) by the relation

$$\alpha(\omega) = \frac{2\kappa(\omega)\omega}{c} \tag{2.25}$$

However, the amount of the absorption inside the medium can be determine by the imaginary part of the dielectric constant. From the Maxwell equation, travelling wave can be expressed as below in the time and Fourier domain, respectively.

$$\nabla \times \nabla \times \boldsymbol{E} = \mu_0 \frac{\partial^2 \boldsymbol{D}}{\partial t^2} \tag{2.26}$$

$$\boldsymbol{K}(\boldsymbol{K}.\boldsymbol{E}) - K^2\boldsymbol{E} = -\varepsilon_r(\boldsymbol{K},\omega)\frac{\omega^2}{c^2}\boldsymbol{E} \tag{2.27}$$

here, $c = \frac{1}{\sqrt{\varepsilon_0\mu_0}}$ is the velocity of light in vacuum. Based on the direction of the polarization of the electric field vector, two cases need to be considered.

For the transverse wave case: $\boldsymbol{K}.\boldsymbol{E} = 0$ and we get the dispersion relationship

$$K^2 = \varepsilon_r(\boldsymbol{K},\omega)\frac{\omega^2}{c^2} \tag{2.28}$$

For the longitudinal wave case: We get

$$\varepsilon_r(\boldsymbol{K},\omega) = 0 \tag{2.29}$$

This equation explains the longitudinal collective oscillation can only occurs when the frequencies corresponding to zeros of $\varepsilon_r(\omega)$ [45].

2.1.2 Plasmonics

There is a lot of interest at present in the plasmonic behavior of nanostructures. In order to discuss plasmonics, an understanding of plasmons is very important. A plasmon is the collective oscillation of the free electrons at the nanostructure surface. To get a clear picture about plasmons, suppose a metal conductor is placed inside an external electric field which is a constant value. Let us say that the electric field pointing to the right. Free electrons will move to the left side as a result the electric field inside the metal conductor goes to zero. If the external electric field is suddenly turned off; the electrons will move to the right towards the positive ions by the Coulomb force but they also repelled by each other because of the same charge. This will cause the electrons to start to oscillate and this oscillation is a damped oscillation. They oscillate at the plasma frequency and this oscillation lasts until the energy is dissipated [49], [50].

Figure 2.1 illustrates the plasmon mechanism when an external electric field is applied on a bulk metal. This electron oscillation is called a bulk plasmon.

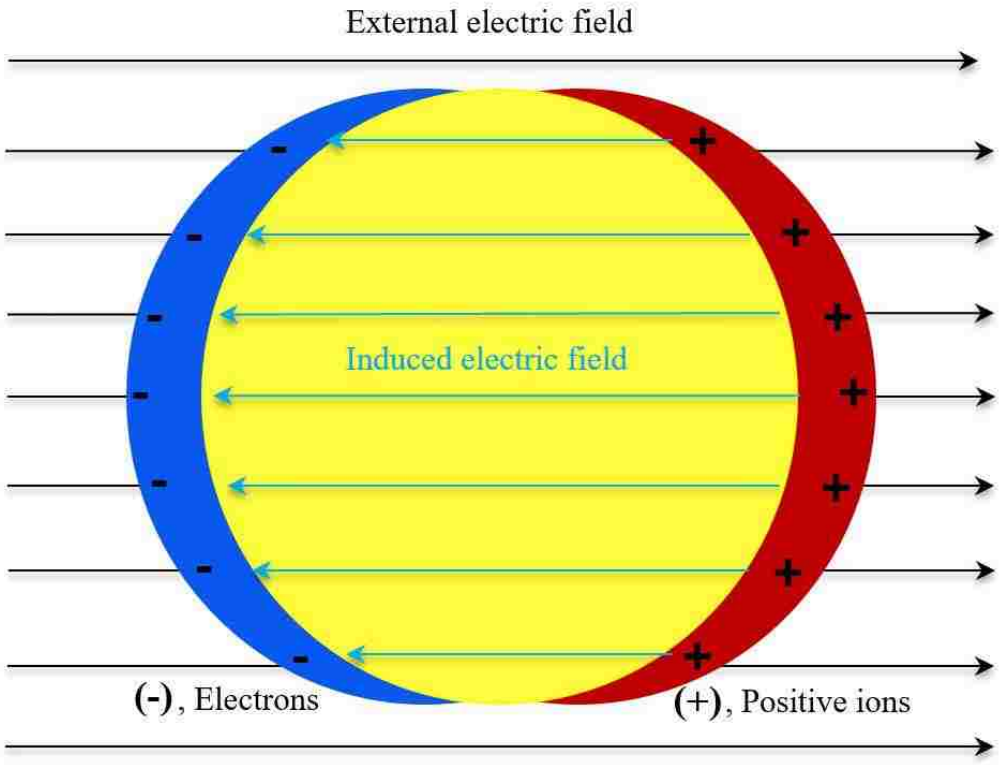

Figure 2.1: Static electric field across gold structure.

Light is an electromagnetic wave. It has both electric and magnetic fields. The fields oscillate as they propagate. Metals behave differently when the light passes through them depending on their size, shape, and surrounding medium. Optical properties of the metal nanostructures are very different than those of bulk structures. When the light interacts with the material, its electric field can exert an oscillating force on the conducting free electrons. For conducting materials, free electrons are present at the surface. When light is incident upon the surface of a metal, tangential oscillating fields along the surface can move the electrons back and forth, and produce longitudinal charge density waves. These waves are surface plasmons. Surface plasmons can produce local electric fields around the surface. The strongest field enhancement occurs close to the edges or in gaps between the nanostructures. Surface plasmons show resonant behavior at specific incident light frequencies. This frequency or wavelength is

known as the surface plasmon resonance frequency or the surface plasmon resonance wavelength [49].

2.1.3 Localized surface plasmon resonances (LSPR)

In the visible to near-infrared (NIR) electromagnetic region, metal nanostructures show unique optical resonances. Electrons of the metal nanoparticles have resonant responses to the electric field of the light [22], [51], [52]. The Drude model describes the free electron response based on the dielectric function [2], [22].

$$\varepsilon_{Drude} = 1 - \frac{\omega_p^2}{\omega^2 + i\gamma\omega} \tag{2.25}$$

here ω is the incident light frequency, γ is the electron collision frequency in the bulk nanostructure, and ω_p is the plasma frequency of the free electrons. Plasma frequency can be calculated using the free electron density N in the metal and the effective mass m_e of the electrons as:

$$\omega_p = \sqrt{\frac{Ne^2}{\varepsilon_0 m_e}} \tag{2.26}$$

Bound electrons have contribution to get the dielectric function. With the Drude model, a high frequency of the dielectric function part was added to get the good response for the electrons in the incident electromagnetic field [22], [53].

$$\varepsilon_r = \varepsilon_\infty - \frac{\omega_p^2}{\omega^2 + i\gamma\omega} \tag{2.27}$$

When the light illuminates the nanoparticles, the electric field induces waves of collective electrons oscillations on the surface. This phenomenona is called localized surface plasmon resonance (LSPR). Different order of resonance modes are included with this wave depending on the size and shape of the nanostructures. Each mode has a different frequency. If the size of the

particle is less than the light wavelength then it is considered that oscillation of the electrons is dipolar in nature [22], [54]. Using dipolar polarizability, α [22], [55], the collective oscillation of the electrons can be described.

$$\alpha = (1 + \kappa)\varepsilon_0 V \frac{(\varepsilon_r - \varepsilon_m)}{(\varepsilon_r + \kappa\varepsilon_m)} \tag{2.28}$$

here V represents the volume of the nanostructure. The dielectric constant of the medium is defined by ε_m, the shape factor is defined by κ. Shape factor depends on the geometry of the surface where electrons are oscillating [11]. For different shapes, shape factors are different; for example, for a sphere κ =2. The case of maximum α means there is a strong resonance between the free electrons and the incident light. The condition at which polarizability gives maximum value at specific frequency is given by:

$$R_e(\varepsilon_r(\omega)) = -\kappa\varepsilon_m \tag{2.29}$$

where R_e represents the real part of the dielectric constant. This specific frequency denoted as ω_{sp}, corresponds to the localized surface plasmon resonance (LSPR) frequency of the nanostructure. Finally, the localized surface plasmon resonance frequency can be determined by the bulk plasma frequency (ω_p) of the free electrons, geometry of the nanostructure (κ) and dielectric constant of the surrounding medium (ε_m).

$$\omega_{sp} = \sqrt{\frac{Ne^2}{m_e\varepsilon_0(\varepsilon_\infty + \kappa\varepsilon_m)}} \tag{2.30}$$

The resonance frequency corresponding to the electron resonance frequency is determined by the real part of the dielectric function whereas imaginary part of the dielectric function contributes to the broadening and absorptive dissipation of the electron resonance [22].

2.1.4 An analytical approach of light scattering from the rectangular nanostructure

An analytical approach is performed by Massa *et al.* to calculate the scattering, absorption and extinction coefficient. According to [24], a rectangular cuboid of volume *V* with length L_a = *2a*, width L_b = *2b*, and L_c = *2c* was considered. Its center is placed at the origin of the three dimensional coordinate system. The material properties of a rectangular cuboid are defined as a wavelength dependent, complex dielectric function ε, and the cuboid is surrounded by a background material with a dielectric constant ε_b. A plane electromagnetic wave,$\boldsymbol{E}(\boldsymbol{r}) = \boldsymbol{E_0} e^{ik_B z}$ is used as an incident wave, and as a time varying field, $e^{-i\omega t}$is used. The polarization of the incident electric field is along the *x* direction, and the background wave vector is k_B and it is expressed as:

$$k_B = \sqrt{\varepsilon_B} k_0 = \sqrt{\varepsilon_B}\, \omega/c \tag{2.31}$$

Green function formalism [24] is used after the first analytical expression called the Meier-Wokaun approach[56]. The formalism is used from [57], [58] to get the expression for the scattered field in the far field. It is assumed that the field inside the cuboid is constant, and the field at the central point is obtained from the Meier-Wokaun formalism. By considering the depolarization effect in the volume and charges induced at the vertices, the field at the central point is calculated. The electric field inside the cuboid is calculated and can be expressed as

$$E_{x,int} = \frac{E_0}{1 - \frac{\varepsilon_r - \varepsilon_B}{4\pi\varepsilon_B}\left[-2\Omega - \delta + \frac{k_B^2}{2}\beta + \frac{16}{3} i k_B^3 abc\right]} \tag{2.32}$$

where Ω is the solid angle subtended by the side perpendicular to the polarization axis of the rectangular cuboid. Ω is expressed as

$$\Omega = 4 \arcsin\left(\frac{bc}{\sqrt{(a^2 + b^2)(a^2 + c^2)}}\right) \tag{2.33}$$

β, is the geometrical depolarization factor, expressed as

$$\beta = \int_{-c}^{c}\int_{-b}^{b}\int_{-a}^{a} \frac{1}{\sqrt{x^2+y^2+z^2}}\left(1+\frac{x^2}{x^2+y^2+z^2}\right) dx\, dy\, dz \tag{2.34}$$

δ, takes into account the polarization charges at the planar ends of the cuboid orthogonal to the x direction. It is expressed as

$$\delta = \frac{8abc}{(a^2+b^2+c^2)^{3/2}}\frac{\varepsilon_B}{\varepsilon_r} \tag{2.35}$$

and the term $\frac{16}{3}ik_B^3abc$ is used for the radiative correction to the field. The internal field can be used together with the dipolar expressions for the scattering and absorption cross sections:

$$\sigma_{sca} = \frac{k_B^4}{6\pi}|\alpha|^2 \tag{2.36}$$

And

$$\sigma_{abs} = k_B \Im(\alpha) \tag{2.37}$$

This polarizability, α, is obtained from the moment. $\boldsymbol{p} = \varepsilon_0\varepsilon_B\alpha\boldsymbol{E_0}$ and α can be defined as

$$\begin{aligned}\alpha &= 8abc\,\frac{(\varepsilon_r-\varepsilon_B)E_{x,int}}{\varepsilon_B E_0} \\ &= \frac{8abc}{\frac{\varepsilon_B}{\varepsilon_r-\varepsilon_B}-\frac{1}{4\pi}\left[-2\Omega-\delta+\frac{k_B^2}{2}\beta+\frac{16}{3}ik_B^3abc\right]}\end{aligned} \tag{2.38}$$

Finally, the extinction cross section is defined as

$$\sigma_{ext} = \sigma_{sca} + \sigma_{abs} \tag{2.39}$$

Although using field inside the nanoantenna allows one to calculate the scattering, absorption and extinction cross section from dipolar formula, a more accurate result can be

obtained by considering scattering in the far field using the Green function formalism. Then, the scattering cross section is founded as

$$\sigma_{sca} = \frac{1}{E_0^2}\int dS\, r^2 |E_{sca}^{FF}|^2$$

$$= \frac{k_0^4|\Delta\varepsilon|^2}{15\pi E_0^2}\left\{\frac{8}{63}a^2b^2c^2[1260 - k_B^2(84a^2 + 168b^2 + 168c^2) + k_B^4(3a^4 + 9b^4 + 9c^4 + 4a^2b^2 + 4a^2c^2 + 6b^2c^2)]\left|E_{x,int}\right|^2\right\} \quad (2.40)$$

here, $\Delta\varepsilon = \varepsilon_r - \varepsilon_B$. Also the extinction cross section expressed as

$$\sigma_{ext} = \frac{4\pi}{k_B^2 E_0} R_e\left[\frac{-ik_B r}{e^{ik_B r}} E_{x,sca}\right] = -\frac{k_0^2}{k_B E_0} R_e\left[i\Delta\varepsilon E_{x,int}\right]\left(8abc - \frac{4k_B^2}{3}abc^3\right) \quad (2.41)$$

where R_e is the real part. The absorption cross section can be defines by equation (2.44) [5].

3 Chapter: DEVICE FABRICATION

3.1 Photolithography

The sizes of the electronic devices are getting smaller day by day. The Very Large Scale Integration (VLSI) idea allow us to decrease the size of the devices and also increase the number of devices in a chip. In the micrometer range, photolithography plays an important role. Figure 3.1 shows the principle of photolithography. The light source being used for this process will be ultraviolet light. UV rays are projected through the mask and focused by a lens on the photoresist, and making patterns on it. After exposure to the UV rays, a development process has to be performed.

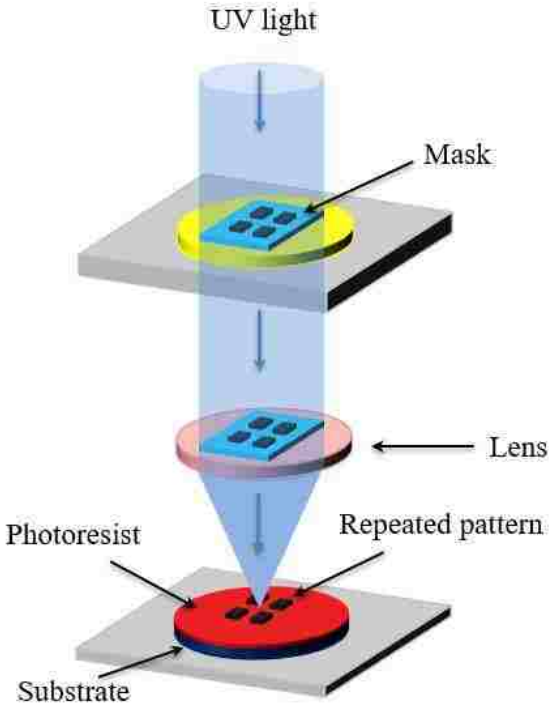

Figure 3.1: Photolithography process using patterned mask.

Then metals are deposited on the sample by the evaporation process. After that, lift-off process is done. Finally, the desired structures are all that remains on the sample substrate.

Photolithography has a diffraction limit. To get a smaller size for the structure than the source light wavelength λ, the numerical aperture of the lens and light wavelength play an important role. From the Airy formula

$$Feature\ size, a = 1.22\ \frac{\lambda}{NA} \tag{3.1}$$

where λ is the source light wavelength and *NA* is the numerical aperture of the lens. *NA* is defined as

$$NA = n\ sin\theta \tag{3.2}$$

where *n* is the refractive index of the surrounding medium and θ is the projection angle. Depending on the two equations, feature size can be decreased by reducing the value of the source light wavelength or increasing the value of the refractive index of the surrounding medium. Using near field lithography, the diffraction limit can be removed. But it is very hard to get sub-100 nm resolution by photolithography. The lower limit for the size of the structure created via photolithography is around 150 nm, which is large for the plasmonic nanostructures. People are using X-ray lithography with a source wavelength of 13.4 nm to get sub-100 nm lithography. But X-ray has some difficulties. It prevents working in transmission, multilayer coating needed for efficient reflective surface, and also it is not good for those are working with it continuously [59], [60], [61].

3.2 Electron Beam Lithography

In 1936, accelerated electrons as an exposure source was proposed for microscopy instead of photons. Due to the lower wavelength value, for 100 keV of energy, the electron wavelength is around 3.9 pm which is smaller than the dimension of an atom [59]. As a result diffraction limit should not be an issue and we may get the images of the atoms. Aberrations and the beam size are fixed by the current probe which is defined by the number of electron per unit time. It can also produce precisely shape nanostructures [59].

De Broglie defines the wave-particle duality of the electrons and the wavelength of the electron is defined by

$$\lambda = \frac{h}{p} \tag{3.3}$$

where, *h* is the Plank constant and *p* is the momentum of the electron.

In the 1960s, Electron beam lithography based on the scanning electron microscopy (SEM) technology was proposed, where accelerated electrons are emitted by an electron gun. There are two types of electron guns normally used in the SEM, those being the thermionic emitter and field emission emitter [62]. For the thermionic emitter, electrons are excited by thermal energy and emit electrons by overcoming the barrier from the filament. In low vacuum, tungsten (W) is common thermionic emitter, while in high vacuum LaB_6 is frequently used. For the field emitter gun, a large electric field is used for emitting the electron beam. Tungsten (W) or carbon nanotubes are commonly used for this emitter. Therefore, 10-50 keV is used between cathode and anode to emit the electron beam. Around 10-50 μm is the beam cross section for the thermionic emitter and 10-100 nm for the field emission emitter. This beam is demagnified by the magnetic lens. By varying the electric and magnetic field as a function of radial position,

electric and magnetic lenses can be made which controls the electrons. Magnetic lenses control the electron beam so that beam diameter makes small spot size.

Unfortunately, these electron lenses have aberrations such as chromatic and spherical aberrations. Chromatic aberration is caused by different wavelength which in this case is different electron energies. Those aberrations cause huge problems for electron beam lithography. To get good size and shape of the nanostructures the aberrations need to be corrected. By reducing the value of the numerical aperture aberrations can be controlled. The resolution (*R*) is defined by the relation

$$R = k_1 \frac{\lambda}{NA} \tag{3.4}$$

where k_1 is the process dependent parameter in the range of 0.4-1.0, and *NA* is the numerical aperture [63]. From equation 3.4, if *NA* is very small the resolution becomes higher. Lower *NA* means lower aberration and higher *NA* causes higher aberration as well as lower resolution. This electron beam produces probe current 10^{-10} to 10^{-12} A on the sample surface.

Electron beam lithography does not need a mask like photolithography to write a pattern on the photoresist. It can write directly on the photoresist. It has computer controlled beam blanking so that the beam can be controlled any time. It has various writing strategies such as raster scan, vector scan and variable shaped beam. Raster scan, scans back and forth and beam blanked is used where it is necessary. It is very easy but slow and here spot size can be adjusted. Using vector scan, beam can be taken where we want to write then performs raster scan and finally beam can come back to its original position. By this scan, only expected area can be exposed. It is relatively faster and used for the sparse patterns. For the case of variable shaped beam, a rectangle is projected to make the pattern.

However, beside all those benefits the electron beam lithography has some problems that limit the resolution of EBL. One of them is spot size, it can be controlled by the wavelength and numerical aperture typically from 0.5 nm to couple of nanometers. Sometimes spot size needs to be bigger for quick writing. Electron scattering inside the photoresist and substrate also can cause problems in writing. Additionally, if the current is too high then electron-electron repulsion can cause problems in resolution.

In this system, the working distance between the final probe-forming lens and the specimen is kept relatively long so that magnetic effects on the sample can be kept at zero. This set-up can cause some problem for the size of the beam.

Electron scattering is very important for the electron beam lithography. Electrons hit the photoresist and substrate and scatter causing a chemical change in the photoresist. Therefore, electron-material interactions play an important role in the electron beam lithography. The most important aspect of electron-material interactions is Rutherford scattering. Due to Rutherford scattering, electrons closer to the nucleus are deflected by the surrounding electron of the atoms. If the energy of the electron is low then it is deflected more than high energy electrons. When electrons are deflected straight back it is called backscattering. Also, when the electron hits the material it ionizes the atom and produces electrons called secondary electrons. These secondary electrons can also produce other secondary electrons. Finally, electrons can lose energy when they pass through the material and can be calculated by the Bethe formula [64].

Scattering mechanisms were combined and modeled by a Monte Carlo simulation model. According to this model, low energy electrons can spread out when it travels down the photoresist. When they hit the high atomic number atom such as Ti / Cr or Si, many more backscattering events happen and electrons lose energy. If some of the electrons pass through the

Si layer they bounce around until they stop. For high energy electrons they pass through the photoresist with low radial spread out but back scattered electrons they travels longer with almost same as incident energy [65], [66]. Long backscatter range can cause problems for the resolution. It can expose features around the expected one. It is called the proximity effect. By controlling beam dose, proximity effect can be controlled.

Figure 3.2 shows the working principle of the E-beam lithography. The electron gun emits the electron beam and the beam is controlled by the magnetic lenses. A focusing lens can focus the electron beam at a point on the specimen with a very low spot size of around 1 nm to couple of nanometers. When the beam strikes the sample it also produces different kinds of scattered electrons. It produces secondary electrons and secondary electrons which are detected by the detector. By controlling the beam spot position and stage positon, writing can be accomplished on the photoresist.

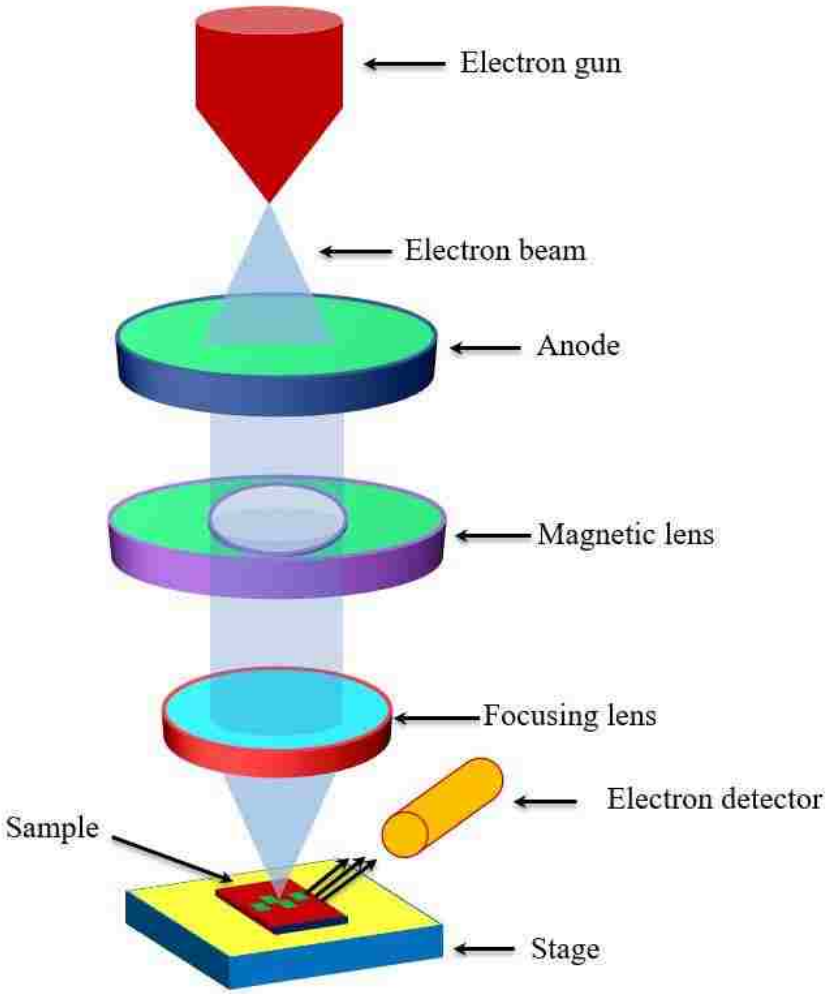

Figure 3.2: Schematic diagram of the E-beam lithography.

3.3 Sample preparation

3.3.1 Wet bench stage:

A silicon (Si) substrate with an oxide layer was chosen as the sample substrate. The substrate chip was cleaned by soaking in acetone for ten minutes. After that the sample chip was sonicated for two minutes. At this stage, the sample chip was rinsed with isopropanol (IPA) and blown dry with nitrogen gas. Then the sample was transferred into spin coater and the vacuum

was turned on in order to hold the sample safely. The sample was centered so that the photoresist distributed evenly over the sample. As a photoresist, Polymethylmethacrylate (PMMA) was used, which is being widely used for electron beam lithography. After centering the sample, two or three drops of A4 PMMA 495 was poured on the center of the sample so that it covers the sample. 3000 rpm speed was maintained for the spin coater for 40 seconds; at this speed PMMA distributes evenly on the sample.

After being coated with PMMA, the sample was transferred to the hotplate. The temperature of the hotplate was maintained at 180°C and the photoresists coated sample was transferred to the hotplate. At 180°C temperature sample was baked for two minutes. The sample was then transferred to the Scanning Electron Microscopy (SEM) chuck. The sample was aligned and held in place with screw and washer. The corner of the sample was scratched by the scriber and numbered so that it can be tracked in the ESEM.

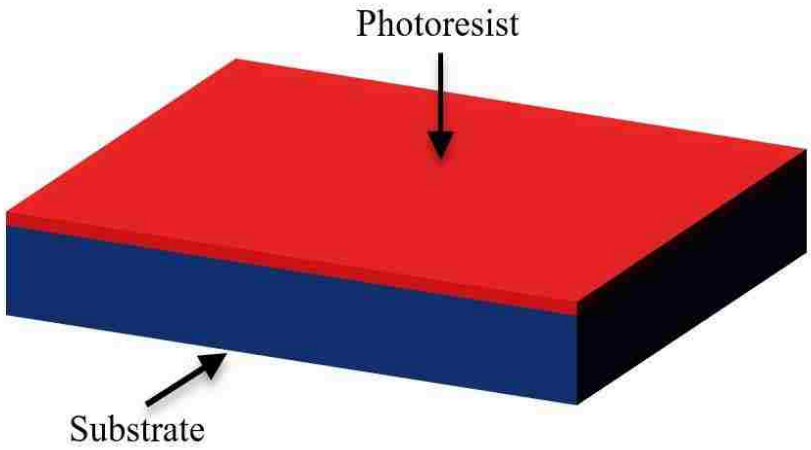

Figure 3.3: Schematic diagram of photoresist coating on the sample substrate

Figure 3.3 demonstrates the sample after spin coating. The red layer is the photoresist on top of the sample substrate and the blue layer is the substrate.

3.3.2 Electron beam lithography stage:

For Electron beam lithography step, the FEI XL30 Environmental Scanning Electron Microscopy (ESEM) was used. In this step, the sample was exposed by the electron beam. For the fabrication process the ESEM was operated by 30 kV and the beam current was 10 ± 0.5 pA.

In the ESEM, the electron beam is being focused into the smallest cone possible so that it can expose the sample surface nicely. Here, electron beam dose plays an important role for controlling the size and shape of the structure. Beam dose exposes the resist area; if the beam dose is larger it will expose a larger area and eventually a large structure will be formed. Dose tests were performed with different wire widths and an optimal area beam dose was determined to be 400 $\mu C/cm^2$. At this facility the minimum size for structures that this ESEM is capable of producing is around 60 nm [49].

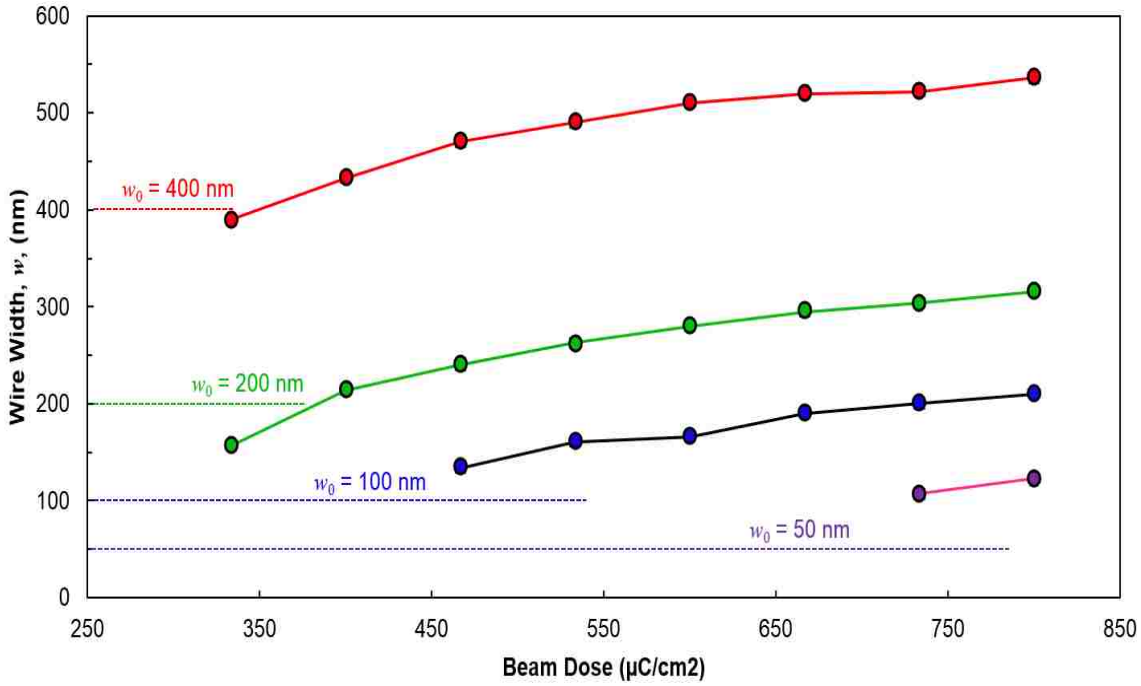

Figure 3.4: Plot of measured structure width vs. electron beam area dose for different nanowire design widths [49].

Figure 3.4 illustrates how the wire width changes with the beam dose. As the beam dose increases, wire-width also increases. Beam doses higher than 400 μC/cm^2 produce larger than expected sizes of the wires. For wire width of 400 nm, 350 μC/cm^2 is the ideal beam dose. As the dose increases, the width also increases. Similar behavior is noticed for 200 nm, 100 nm, and 50 nm. For 50 nm wire width, beam dose less than 740 μC/cm^2 cannot create any structure, only around 100 nm width structure found at the beam dose 740 μC/cm^2. Due to the results from the dose tests, 400 μC/cm^2 was used as the beam dose for the whole fabrication process [49].

Figure 3.5 shows the photoresist being exposed photoresist by the electron beam. Depending on the beam dose and structure size, the electron beam will exposed the desired area.

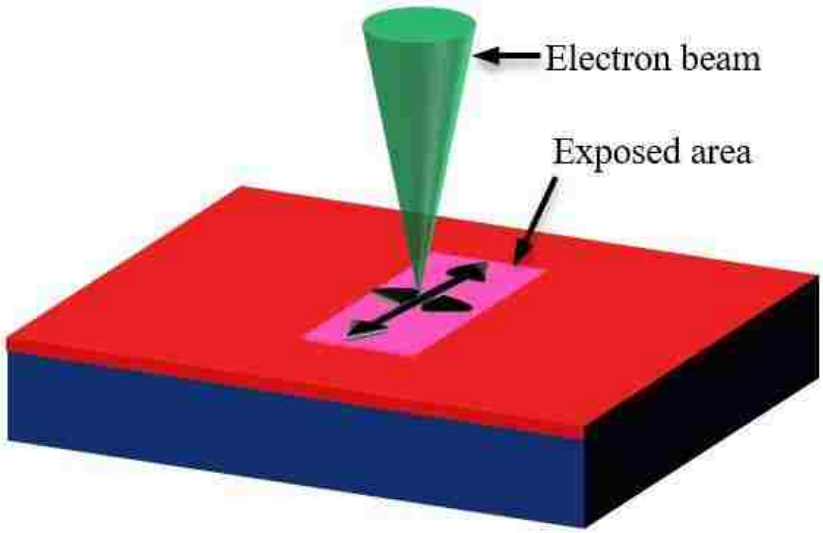

Figure 3.5: Diagram of photoresist exposed by the electron beam.

3.3.3 Development stage:

At this stage, the exposed sample was developed by a developer. To make the developer methyl-isobutyl-ketone (MIBK) solution was mixed with isopropanol. The ratio of developer to solution was 1:3 methyl-isobutyl-ketone (MIBK): isopropanol (IPA) solution.

The exposed sample was put into the developer solution for 40 seconds. After that, it was rinsed with IPA and dried with N_2 gas and the sample readied for the electron beam evaporation stage.

Figure 3.6 is the schematic diagram of the sample after developing with MIBK developer. As shown in the figure, exposed photoresist is washed off by the developer and unexposed resist remains on the top of the sample substrate. The whole idea is to deposit desired materials in the expected shape on the substrate.

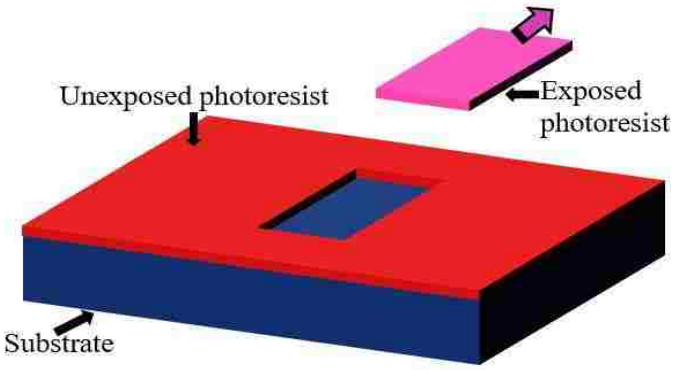

Figure 3.6: Schematic diagram of the sample after sample development.

3.3.4 Electron beam evaporation stage:

At this stage, metals were deposited onto the sample by the electron beam evaporator. Figure 3.7 shows the schematic diagram of the electron beam evaporator. It has a tungsten filament which is heated inside the electron gun. When the tungsten filament gets sufficient hot, it started to emit electrons. Emitted electrons produce a beam and are deflected by the magnet and directed towards the evaporated material holder. The accelerated electron beam strikes the material surface. This results in a large amount of thermal energy being created. Huge numbers of electron strike the material surface and produce more than a million of watt power per square inch. For controlling high heat in the crucible, a water cooling system is installed around it. A high voltage D.C. power supply of around 10 to 30 kilovolts is needed for this operation. When the material surface is struck by the electron beam, the beam vaporizes the target material. Finally metal is deposited on the sample surface. For the whole procedure, high vacuum is mandatory. For our case, system pressure was 1.5×10^{-7} Torr and the temperature was kept as room temperature.

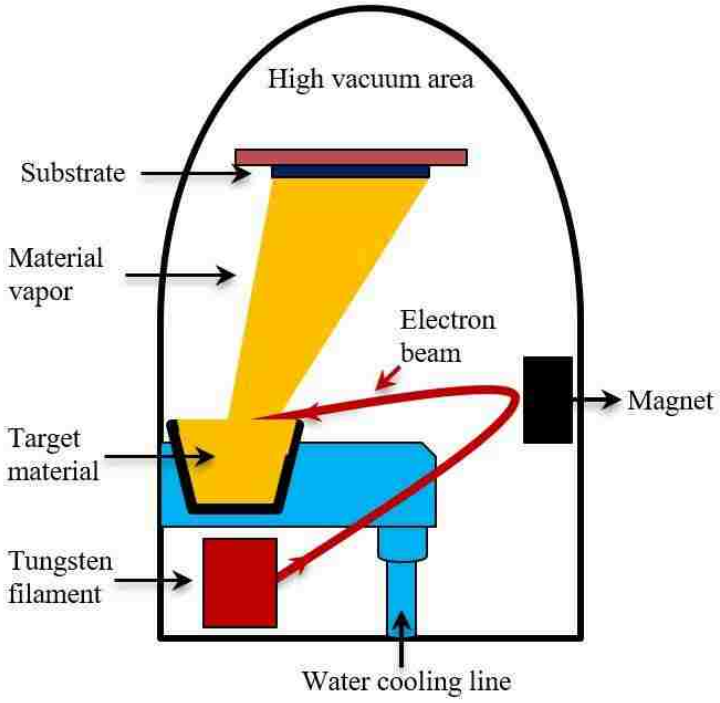

Figure 3.7: Working principle of the electron beam evaporator.

For the whole procedure evaporation rate was maintained 0.5 Å/s and the substrate rotation speed was 16 rpm during the deposition. First, 1.5 nm of titanium (Ti) was deposited as an adhesive layer. An adhesive layer needs to be used because it attaches the material to the sample substrate. As a plasmonic material, gold (Au) was chosen because of its nice response in the visible to near-infrared light regime. Gold thicknesses ware varied from 8 nm to 60 nm.

Figure 3.8 demonstrates the schematic of the sample after gold was deposited by the electron beam evaporator. The thickness of the gold was fixed value for a specific sample. After metal deposition, the sample is ready for cleaning.

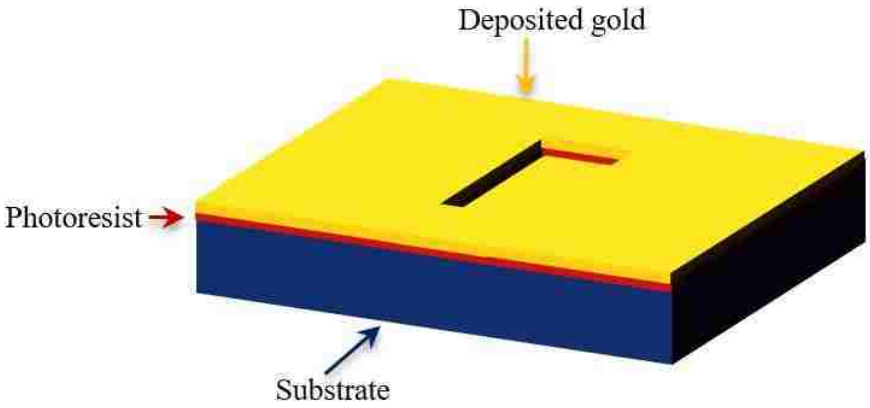

Figure 3.8: Sample after depositing gold by the electron beam evaporator.

3.3.5 Sample cleaning stage:

At this stage, the sample was cleaned by the acetone. First, the sample was put in a vial of acetone and soaked for 10 minutes. During this time, the sample was swirled inside the acetone so that PMMA can be removed easily. After lift-off, the sample was put into IPA and blown dry with N_2 gas. After all those processes, the sample was examined with the microscope to observe the overall quality of the fabricated sample.

Figure 3.9 (a) shows the schematic diagram of the lift-off process. Here, PMMA was removed by the acetone. However, acetone cannot remove the structures attached by the adhesive layer to the substrate. As a result, only metals deposited on the PMMA are removed and the desired nanostructures will stay on the sample substrate, as shown in Figure 3.9(b).

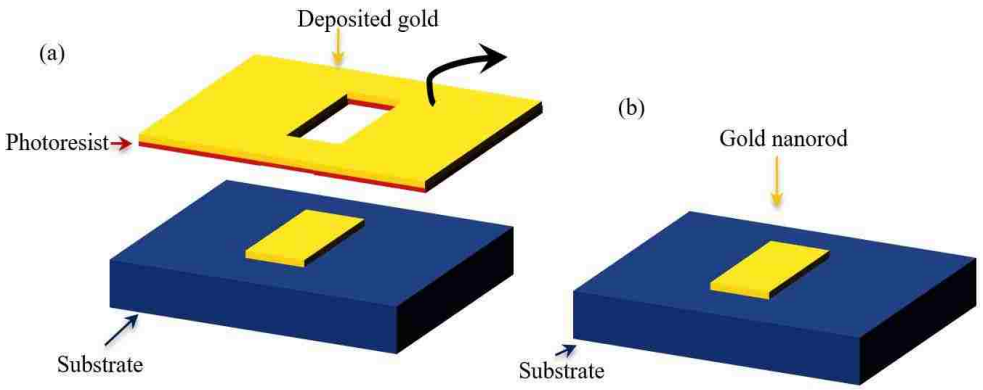

Figure 3.9: Schematic diagram of sample (a) PMMA lift-off stage and (b) fabricated nanostructure.

3.3.6 Sample Imaging:

At this stage, the sample is ready for imaging with the SEM. To get images from the sample, a scanning electron microscopy with FEI Nova Nanolab 200 machine was used. It is an ultra-high resolution low voltage imaging with very low vacuum capabilities. Figure 3.10 (a) shows the SEM images of the nanodisks and nanorods with 20 nm gold thickness. Figure 3.10 (b) and (c) show two nanorods with different lengths and widths.

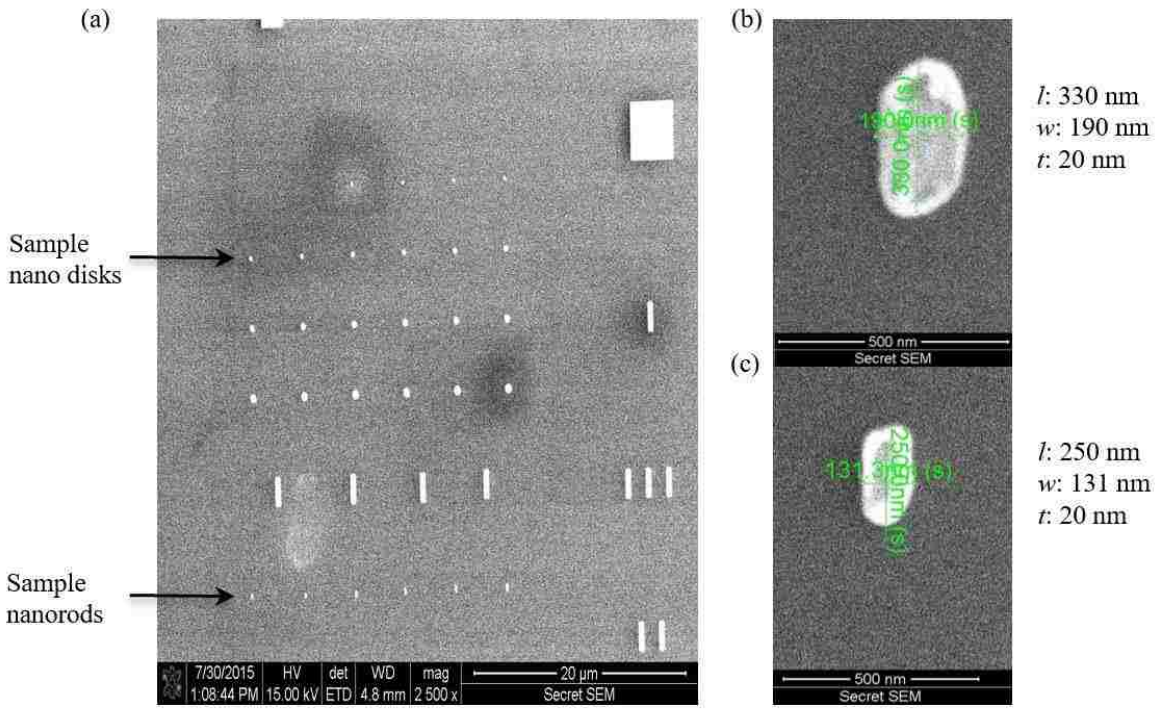

Figure 3.10: SEM images of the EBL fabricated sample

4 Chapter: SIMULATION MODEL

4.1 Model description

Plasmonic studies have been performed on gold nanorods of constant length and width with different thicknesses using finite element method (FEM, COMSOL) simulations. The simulations are performed in three dimensional (3-D) space, where the length of the nanorod is 100 nm, the width is 60 nm and the thickness varies from 8 nm to 60 nm. The dimension of the nanostructure below 100 nm can show very good plasmonic properties. Saylor et al. showed by 2-D FEM simulation, that for a thickness 15 nm and width 60 nm gold nanorod can produce the highest optical enhancement [20]. The substrate effect was approximated by an effective medium n_{eff} = 1.25 around the nanorod which is comparable with a nanorod made by electron beam lithography on a silicon substrate with a silicon dioxide layer [20], [67]–[69]. For the gold nanorods, a Lorentz-Drude wavelength dependent dielectric function has been used. The data for the dielectric function are obtained from Johnson and Christy [70].

A normally incident light was incident onto the surface of the nanorod with the electric field polarized along either the longitudinal or transverse direction. Electric field distribution (EFD), is defined as the ratio of local electric field ($\boldsymbol{E}$) and incident electric field ($\boldsymbol{E_0}$). The electric field distribution, $\boldsymbol{E/E_0}$, was plotted at the resonant wavelength for each thickness. The optical enhancement, defined as the ratio of the local electric field to the incident electric field squared (E^2/E_0^2), was studied. This optical enhancement is related to the local intensity, as intensity is proportional to the electric field squared. For the simulation, two types of rectangular nanorods, sharp-corner and round-corner, were investigated. Absorption of the nanorods was calculated using the heat loss in the volume of the nanorods. Finally, three dimensional charge distributions were calculated according to the Gauss's law in Figure 5.3 and Figure 5.4.

Figure 4.1 illustrates the model cross section. Here, the light has normal incident and the polarization is along the long axis of the sample. Longitudinal and transverse polarizations were used depending on the study. The yellow rectangle represents the gold sample. The size of the sample is 100 nm x 60 nm x *t* nm. In this study, thickness (*t*) is varied from 8 nm to 60 nm. Around the sample an integration space has been defined as the near-field region where most of the enhancement occurs. The radius of the integration space is 125 nm. In this integration space the enhancement of the nanorod was calculated.

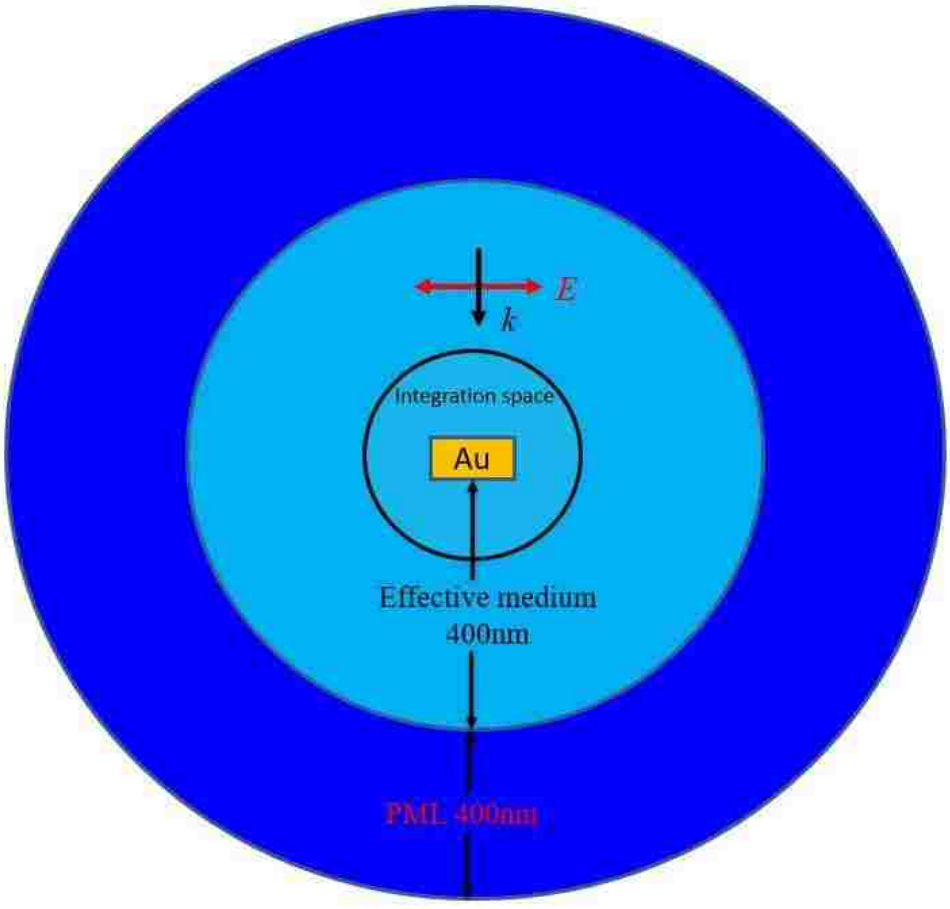

Figure 4.1: Schematic diagram of a cross-section of the simulation geometry of the model.

Around the sample, a 400 nm radius sphere was drawn as an effective medium. The value of the effective medium was approximated by n_{eff} = 1.25 [20], [67], [68]. The effective medium was approximated to create the same environment as the Si substrate with a SiO_2 layer on the top of it. A perfectly matched layer (PML) layer with a 400 nm thickness was used at the boundary of the model. This layer acts as an absorber and should absorb almost all of the outgoing light [71].

Material properties are very important in plasmonic research. The dielectric constant of the gold material depends on the frequency of the light. The dielectric constant also known as relative permittivity, is denoted as $\varepsilon(\omega)$.

$$\varepsilon_r(\omega) = \frac{\tilde{\varepsilon}(\omega)}{\varepsilon_0} \tag{4.1}$$

where $\tilde{\varepsilon}(\omega)$is the absolute permittivity which depends on the frequency; it has a real and imaginary part. The dielectric constant is defined as,

$$\varepsilon_r(\omega) = \varepsilon_1(\omega) + i\varepsilon_2(\omega) \tag{4.2}$$

where $\varepsilon_1(\omega)$ is the real part and $\varepsilon_2(\omega)$ is the imaginary part of the dielectric function. Experimentally, the dielectric constant can be determined by the reflectivity and the complex refractive index. The refractive index $\tilde{n}(\omega)$ of the medium can be defined as

$$\tilde{n}(\omega) = n(\omega) + ik(\omega) \tag{4.3}$$

From this frequency dependent refractive index at the optical frequency, the dielectric constant can be determined using the relationship between refractive index and dielectric constant.

$$\varepsilon_r(\omega) = \tilde{n}^2 = \big(n(\omega) + ik(\omega)\big)^2 \tag{4.4}$$

$$\varepsilon_1(\omega) = n^2 - k^2 \tag{4.5}$$

$$\varepsilon_2(\omega) = 2nk \tag{4.6}$$

Using equations (4.5) and (4.6), the optical frequency dependent real and imaginary values of the dielectric function were calculated [45], [72]–[75]. Using data from Johnson et al [70], the dielectric constant is reproduced and plotted in Figure 4.2. The vertical axis represents the imaginary part in (a) and the real part in (b) of the dielectric function. The horizontal axis represents the wavelength. This wavelength dependent dielectric function has been used for the whole simulation.

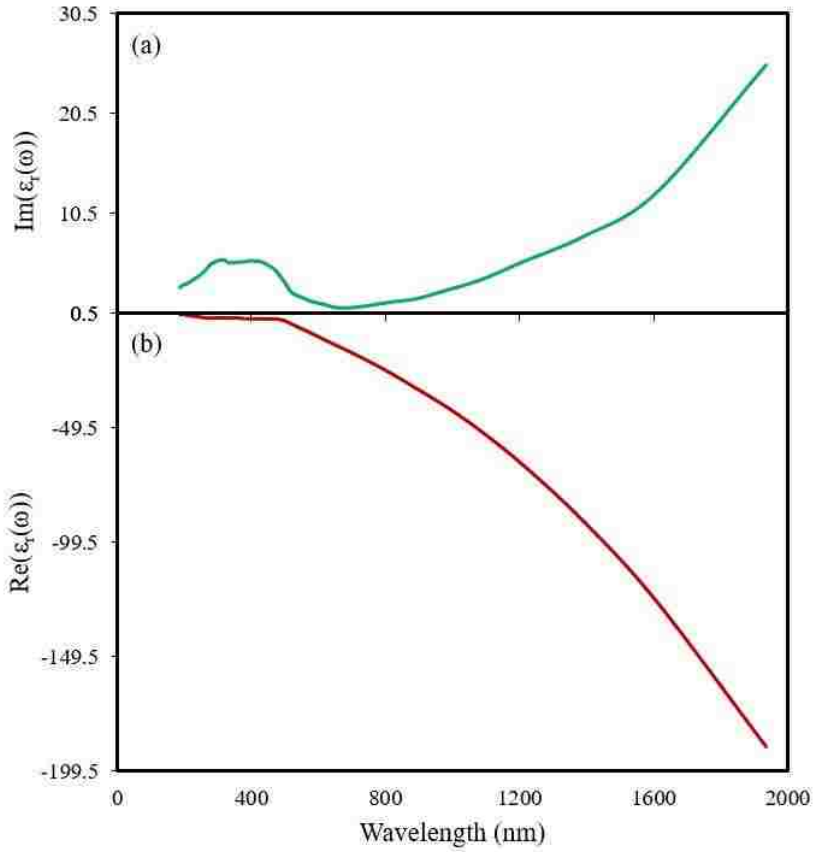

Figure 4.2: Complex dielectric function of gold as a function of wavelength (a) Imaginary and (b) real parts reproduced using data from Johnson et al [70], [76].

Meshing is very important for the finite element method. A smaller mesh sizes can improve the results. For this simulation, three different sizes of mesh size were used. For the perfectly matched layer (PML) and the effective medium the minimum mesh size used was 18 nm and the maximum mesh size for both cases was 80 nm. For the integration space, the minimum mesh size used was 1 nm and maximum mesh size used was 10 nm. Finally, for the nanostructure the minimum and maximum mesh sizes used were 1 nm and 5 nm respectively. Figure 4.3 shows the different mesh sizes for the different layers of the simulation model. Figure 4.3(a) shows the meshing in the perfectly matched layer (PML). Figure 4.3(b) demonstrates the meshing in the effective medium. Figure 4.3(c) shows the meshing in the integration space And Figure 4.3(d) shows the meshing in the sample.

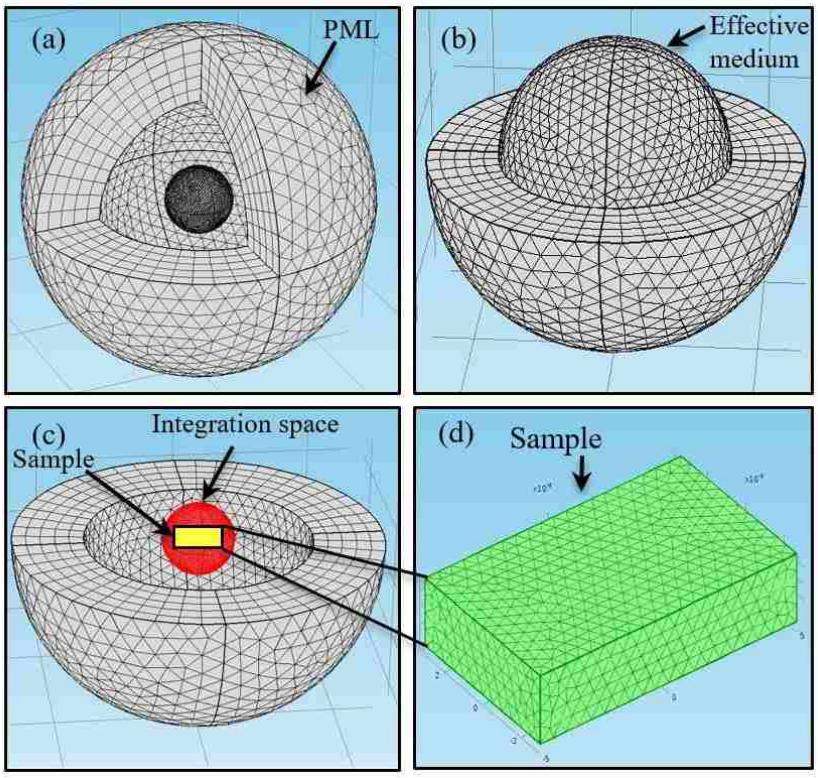

Figure 4.3: Mesh size for (a) Perfectly matched layer (PML) (b) Effective medium (c) Integration space (d) Sample.

The total absorbed energy calculated using the heat loss inside the nanostructures as

$$W_{abs} = \iiint Q_{abs} dV = \frac{1}{2} \iiint R_e[(\sigma \boldsymbol{E} + j\omega \boldsymbol{D}).\boldsymbol{E}^* + j\omega \boldsymbol{B}.\boldsymbol{H}^*] dV \tag{4.7}$$

And total scattered energy

$$W_{sca} = \oiint \mathcal{P}_{sca}.\boldsymbol{n}\, ds = \frac{1}{2} \oiint R_e[\boldsymbol{E}_{sca} \times \boldsymbol{H}^*_{sca}] \tag{4.8}$$

Also the absorption and scattering cross-section can be defined as

$$\sigma_{abs} = \frac{W_{abs}}{\mathcal{P}_{inc}} \tag{4.9}$$

and

$$\sigma_{sca} = \frac{W_{sca}}{\mathcal{P}_{inc}} \tag{4.10}$$

The enhancement calculated as

$$= \int E^2 dV \tag{4.11}$$

4.2 Model comparison

4.2.1 Model compared with Giannini et al.

The simulation model was tested with experimental results by creating a similar environment as that discussed by Giannini et al [32]. They have made their sample (rectangular nanorod) using electron beam lithography and physical vapor deposition. Computational results were obtained using the same parameters as [32]. Figure 4.4 shows experimental and simulation results for the gold nanostructures. The scattering resonant wavelength was plotted as a function of the long-axis length where the width and height of the nanostructures are 123 nm and 13 nm, respectively.

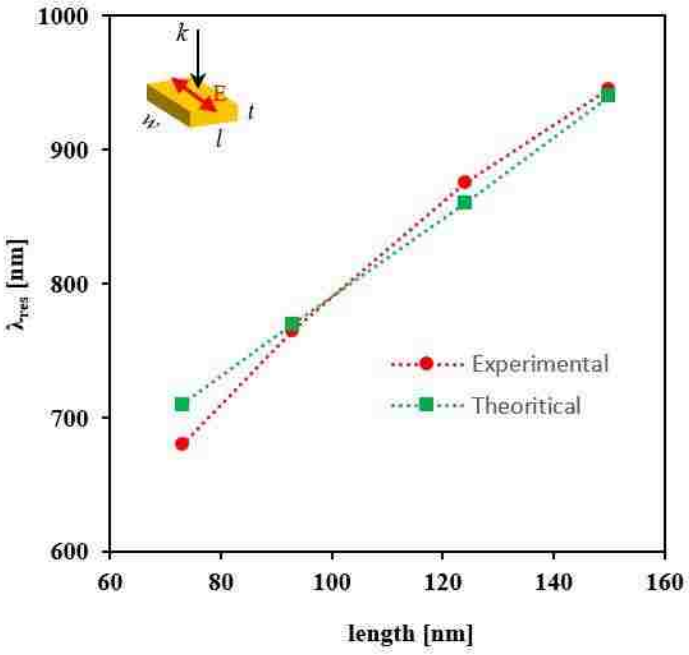

Figure 4.4: Simulation results comparison with the experimental results [32].

From Figure 4.4, it is clear that the simulation results closely match with experimental results.

4.2.2 Model compared with Langhammer et al

Experimental results from Langhammer et al. also reproduced by simulation [27]. Figure 4.5 (a) shows the simulated result and Figure 4.5 (b) shows the experimental result from [27]. Both plots show that the resonant peak energy closely matches. After normalization, it is clear that they have some intensity mis-match, but it is normal because experimental procedure causes some loss of intensity.

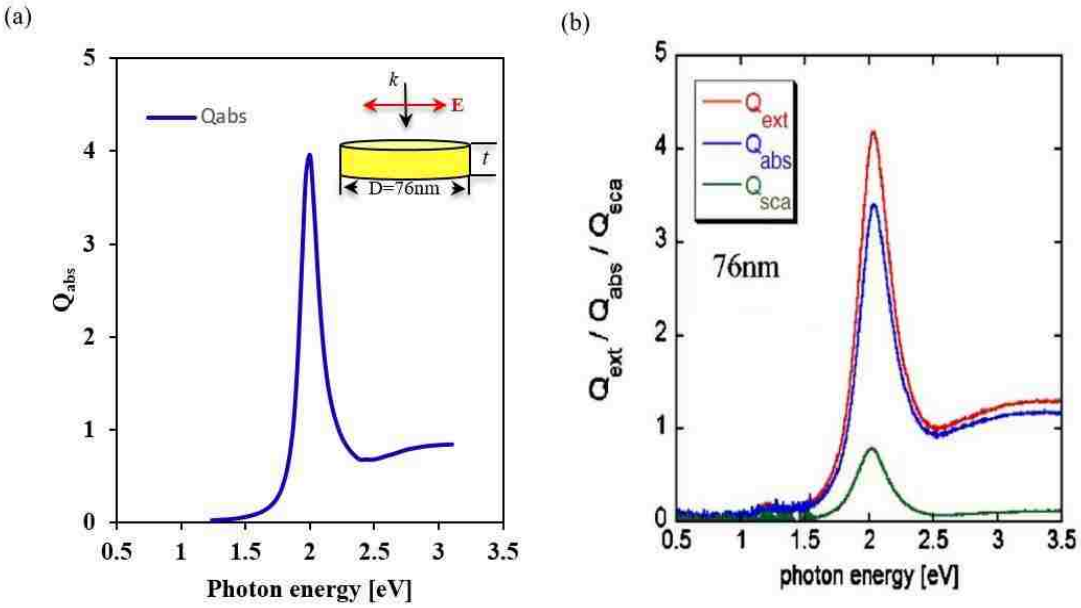

Figure 4.5: Scattering, absorption and extinction efficiency for gold nanodisc with 76 nm diameter, 20 nm thickness (a) simulation result and (b) measured result [27].

5 Chapter: SIMULATION RESULT AND DISCUSSION

The absorption of the nanorods was determined with thickness variation. The absorption spectra of various thicknesses were plotted as a function of incident light wavelength. Figure 5.1 (a) shows the absorption spectra when the polarization is aligned along the longitudinal axis. Each line on the plot indicates the spectrum of a single nanorod with a particular thickness. The nanorods lengths and widths were kept constant at 100 nm and 60 nm respectively and the thicknesses ware varied from 8 to 60 nm. The plot shows that for both polarizations the absorption resonance peak shifts toward blue as the thickness increases. Figure 5.1(b) shows the absorption for the transverse polarization using the same parameters; the observed trend is the same but the amplitude is reduced compared to the longitudinal polarization. The resonance peak value comparing the two polarizations for the same geometrical parameters gives different position. For longitudinal polarization the resonance wavelength value is larger than for the transverse polarization because plasmonic response depends on the coupling effect of surface plasmons [77]. The shape or FWHM of the spectrum also increases with increasing thickness. Figure 5.2 shows the optical enhancement spectra for nanorods of constant length and width with different thicknesses. Optical enhancement was plotted as a function of incident light wavelength for both longitudinal and transverse polarizations. Figure 5.2 (a) indicates that the enhancement peak shifts towards blue with increasing thickness as shows in Figure 5.1 for the absorption.

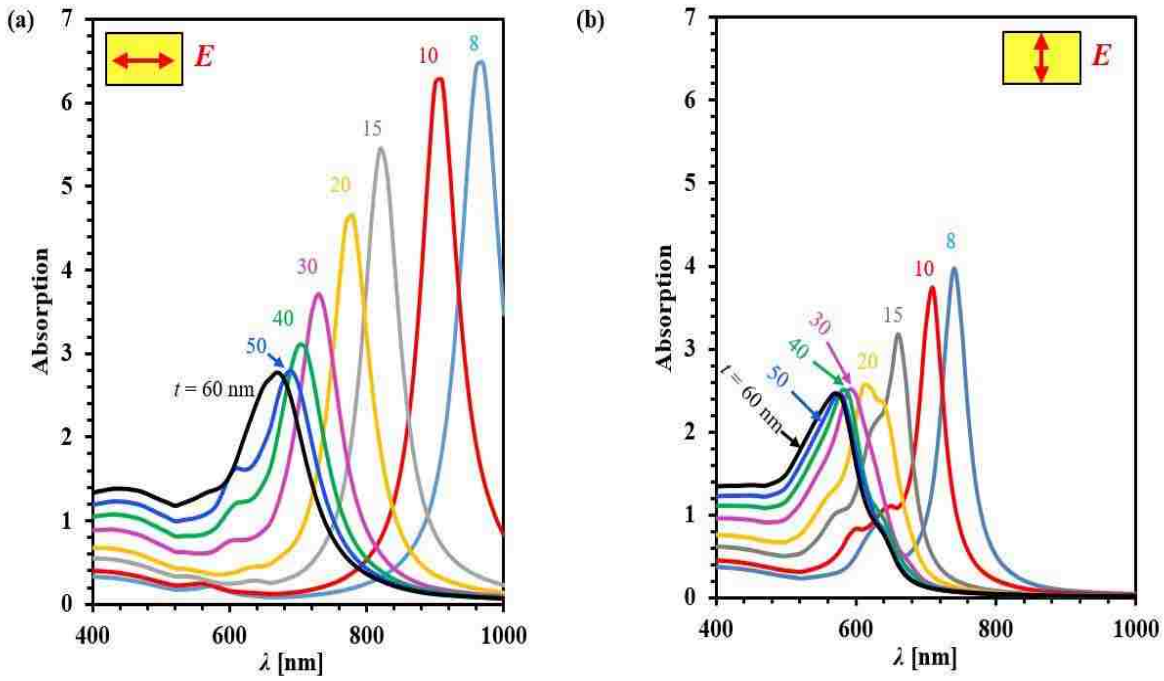

Figure 5.1: Calculated absorption spectrum of 100 nm length and 60 nm width sharp-corner rectangular gold nanorod with different thickness for (a) longitudinal polarization and for (b) transverse polarization. In both cases light is normally incident and the value of the effective medium used, n_{eff} = 1.25.

For a thickness of 8 nm and longitudinal polarization the resonance peak at 970 nm whereas for transverse polarization the resonance peak is at 740 nm. Peak resonance wavelength has different values for the same nanorod with different polarizations. However, the value of the optical enhancement decreases with increasing thickness for both polarizations. Electric field distributions (EFD) of different thickness for the sharp-corner and round-corner rectangular gold nanorods shown in Figure 5.3(a) and figure 5.4(a) respectively.

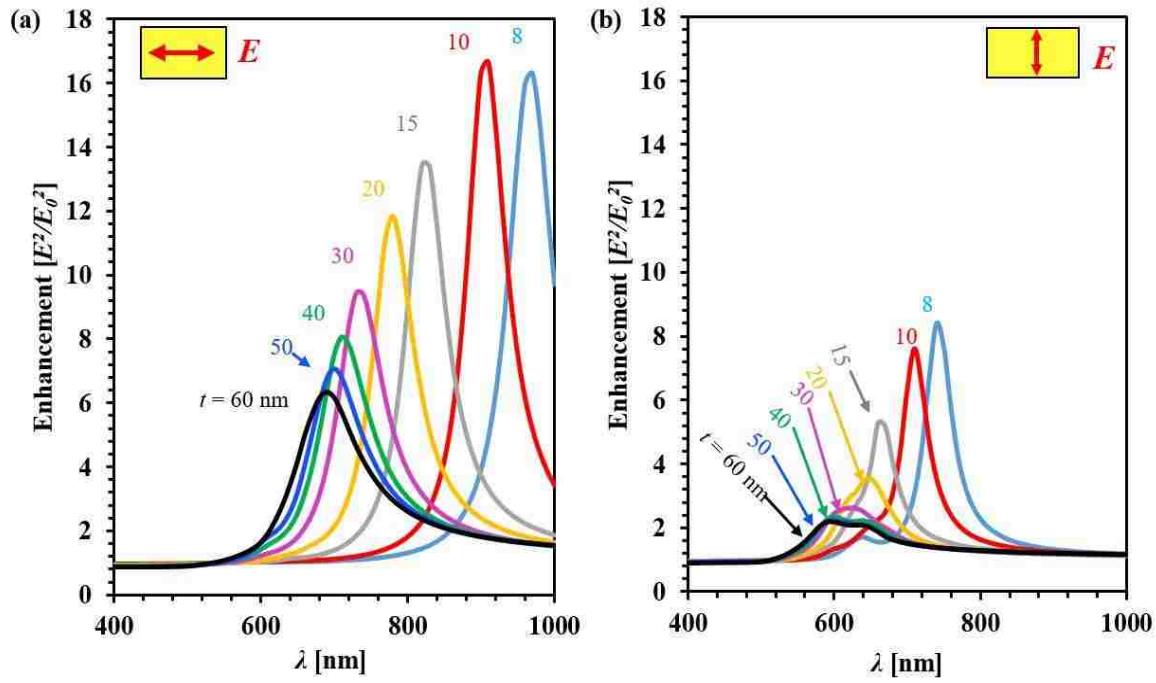

Figure 5.2: Calculated average enhancement (E^2/E_0^2) spectrum in the integrated volume of sharp-corner rectangular gold nanorod for normal light incidence in the effective medium (n_{eff} = 1.25) with different thickness for (a) longitudinal polarization (b) transverse polarization.

For sharp-corner rectangular nanorod, Figure 5.3 (a) shows that at top and bottom surfaces electrons are tend to gather toward the corner of the nanorod because the electric field of the incident light applies a force on the electrons. The electric field distribution behaves like a quadrupole distribution. For round-corner rectangular nanorod, Figure 5.4 (a) shows that surface electrons are evenly distributed and look more like a dipole distribution. The amplitude of electric field distribution decreases as the thickness increases.

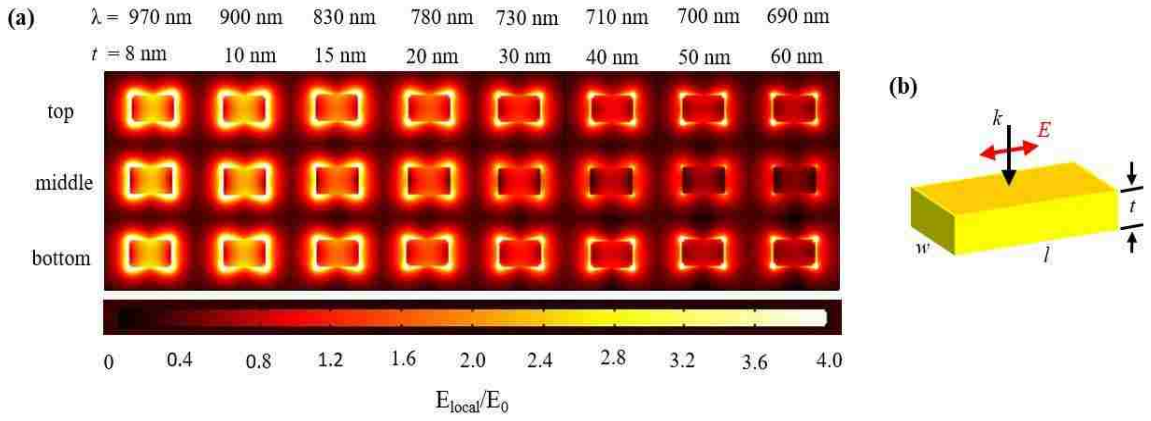

Figure 5.3: (a) Electromagnetic field distributions (EFD) for top, middle and bottom surfaces at resonance wavelengths for sharp corner Au nanorods of length 100 nm and width 60 nm for different thickness when polarization is aligned along the long axis and normal incidence.

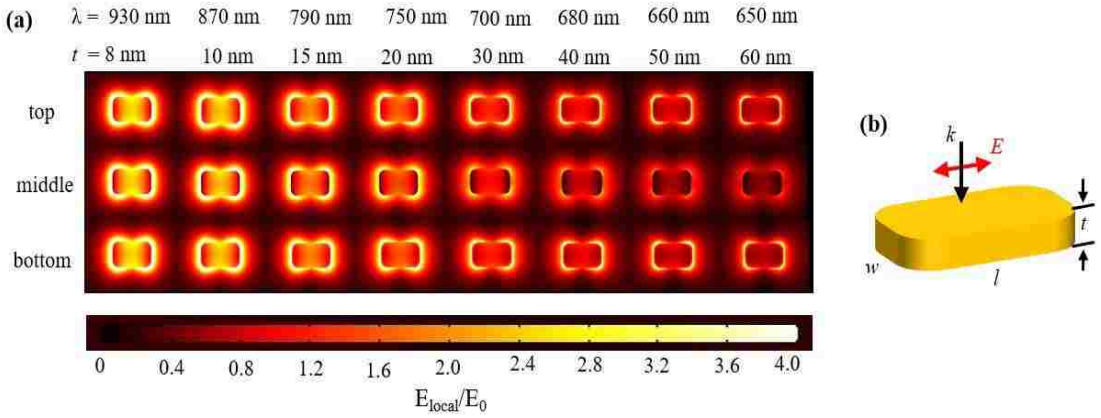

Figure 5.4: (a) Electromagnetic field distributions (EFD) for top, middle and bottom surfaces at resonance wavelengths for round corner Au nanorods of length 100 nm and width 60 nm for different thickness when polarization along the long axis and normal incidence. (b) Schematic of round corner nanorod.

Figure 5.5 (a) shows maximum enhancement of sharp and round corner structures with longitudinal and transverse polarizations as a function of thickness. Maximum enhancement decreases with increasing thickness. For sharp corner and round corner structures the maximum

enhancement has a definite difference. For longitudinal polarization, maximum enhancement decreases quickly and tends to stable value at higher thickness. For transverse polarization and for both shape, maximum enhancement decreases quickly up to 20 nm thickness after that it does not change so much and get constant value. For both polarizations and shapes the maximum enhancement has a tendency to decrease its amplitude nonlinearly.

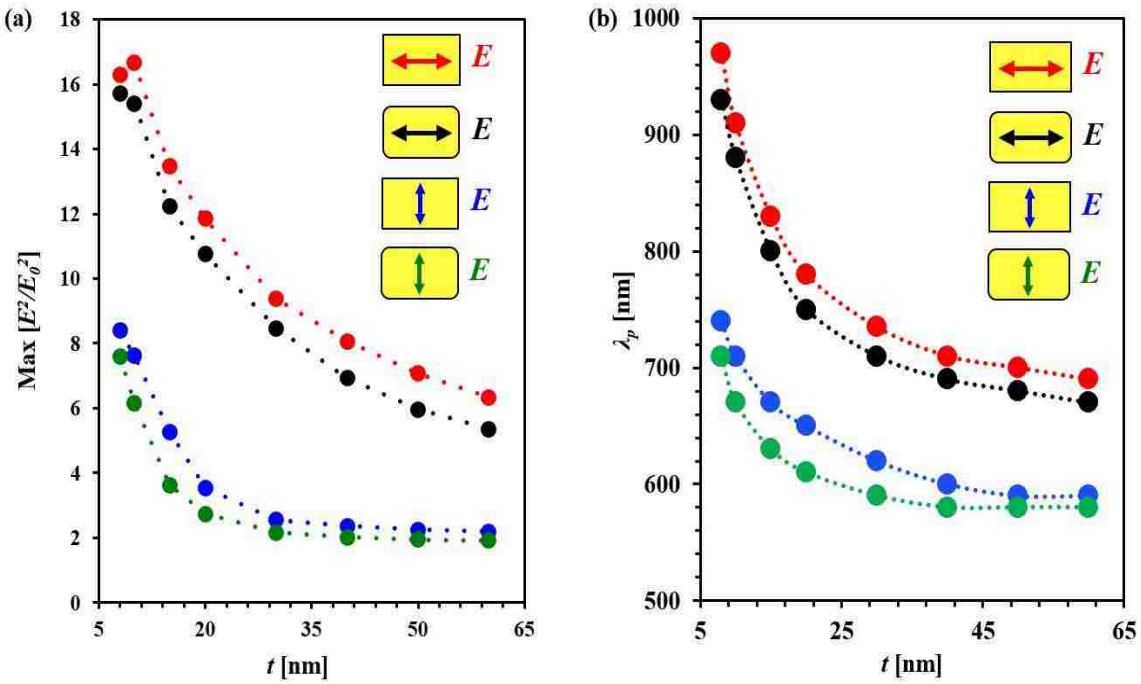

Figure 5.5: (a) Normalized maximum enhancement at resonant incident wavelength as a function of thickness for sharp and round corner nanorods for longitudinal and transverse polarization (b) Peak resonance wavelength as a function of thickness for sharp and round corner nanorods for both longitudinal and transverse polarization.

Figure 5.5 (b) indicates the peak resonance wavelength for the enhancement spectrum as a function of thickness. Peak resonance wavelength shifts toward blue when the thickness increases for the both polarizations for both and sharp and round corner shapes of nanorods.

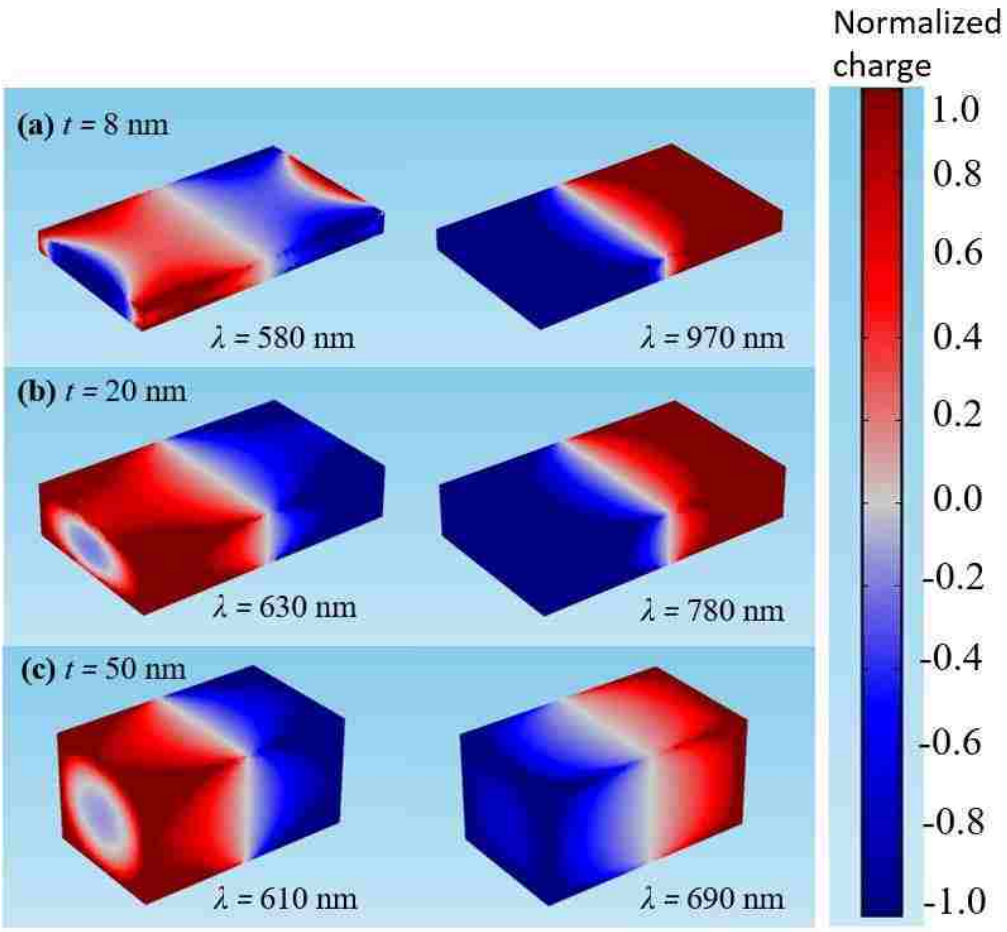

Figure 5.6: Surface charge distributions at peak resonance wavelength when thickness (a) 8 nm (b) 20 nm and (c) 50 nm.

Figure 5.6 demonstrates the surface charge distributions at their resonance modes for three different thicknesses. Using Gauss's law surface charge density was calculated. From the Gauss's law

$$\Phi_E = \frac{Q}{\varepsilon_0} = \oiint (\boldsymbol{n}.\boldsymbol{E})dS = \oiint (\boldsymbol{n_x}.\boldsymbol{E_x} + \boldsymbol{n_y}.\boldsymbol{E_y} + \boldsymbol{n_z}.\boldsymbol{E_z})\, dS \tag{5.1}$$

Where Φ_E is the electric flux is passes through the metal surface S [35]. For our case n_{eff}^2 was multiplied to get the actual surface charge distribution because the value of the effective medium is n_{eff}^2. Figure 5.6 demonstrates the plasmon modes at different resonance wavelength.

Figure 5.6(a) shows the surface charge distribution for 8 nm thickness; there exists, one mode at wavelength 580 nm which clearly shows as quadrupole mode and another mode at wavelength value 970 nm which is a perfect dipole mode. Similar behavior is found for 20 nm and 50 nm thickness.

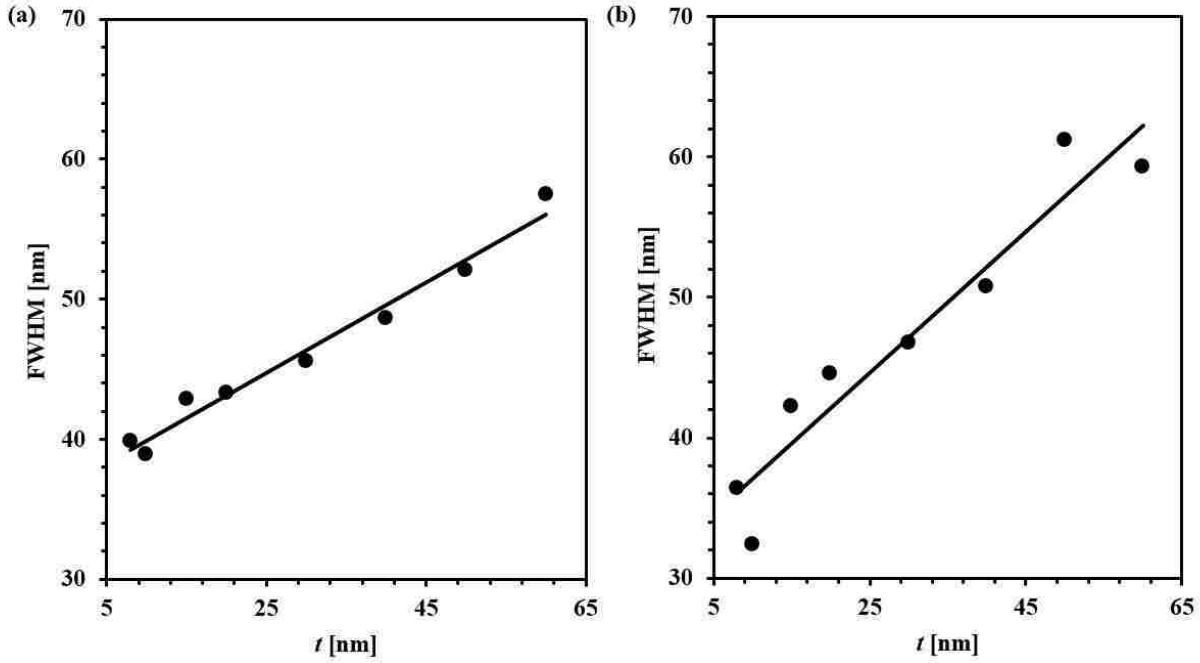

Figure 5.7: Full width half maximum as a function of thickness for (a) enhancement spectrum and (b) absorption spectrum.

Figure 5.7 plots the full width half maximum (FWHM) of the broadening of the enhancement and absorption spectra as a function of thickness. For both cases, plots show that FWHM increases linearly as thickness. Enhancement and absorption spectrum broaden with the thickness of the structure. A larger FWHM value means that the oscillation wavelength is larger. As the thickness increases the absorption resonance wavelength also increasing. Similar behavior exhibited by the enhancement spectrum. Figure 5.8 describes FWHM as a function of resonance

energy. For absorption and enhancement the figure shows nonlinear behavior with resonance energy. For the plasmonic nanostructure, two types of decay occurs for the electrons those being radiative decay and nonradiative decay. Radiative decay produces photons and nonradiative decay occurs as intraband excitation and interband excitation [1] . For gold nanorods, dephasing time (T_2) plays an important role. Dephasing time (T_2) is defined as $T_2 = 2\hbar/\Gamma$, where Γ is the linewidth. It varies widely for different shapes and sizes of nanostructures [1],[21].

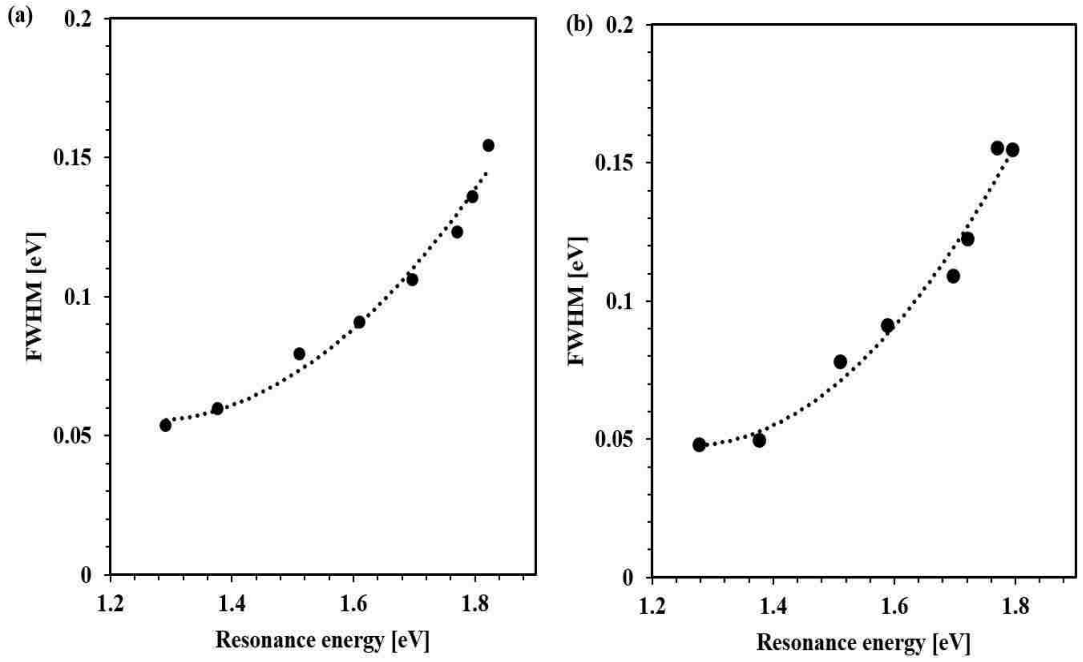

Figure 5.8: Full width half maximum as a function of thickness for (a) absorption spectrum and (b) enhancement spectrum.

Figure 5.8 provides an interesting result as thickness was changed. Here plasmon resonance width (FWHM) was changed for both absorption and enhancement for the nanorods where thickness was varied instead of length and width. It shows a similar trend to that Y-H Qiu et al. [21] where plasmon width was plotted as a function longitudinal surface plasmon resonance (L-SPR) energy where gold nanorod length was changed. From Figure 5.8 (a), it indicates clearly

that as the thickness increases and the surface plasmon resonance energy increases around 1.8 eV the FWHM increases. This broadening is because of interband excitation induced damping where the interband transition threshold energy for gold is around 1.8eV [21]. In plasmon relaxation dynamics, a three level system was introduced by Y-H Qiu et al. According to this system, a fixed frequency is used to excite the electron from ground state to the second excited state where the probability of transition is σ_o and plasmon absorption cross-section was indicated by intensity *I*. A two-steps process is used by electrons to go to the ground state; first the electron transition from second excited state to the first excited state then from first excited state to the ground state. From the second excited state to the first excited state goes through a process called electron-phonon relaxation, and from the first excited state to the ground state the electron transitions with decay rate representing the phonon-phonon relaxation process.

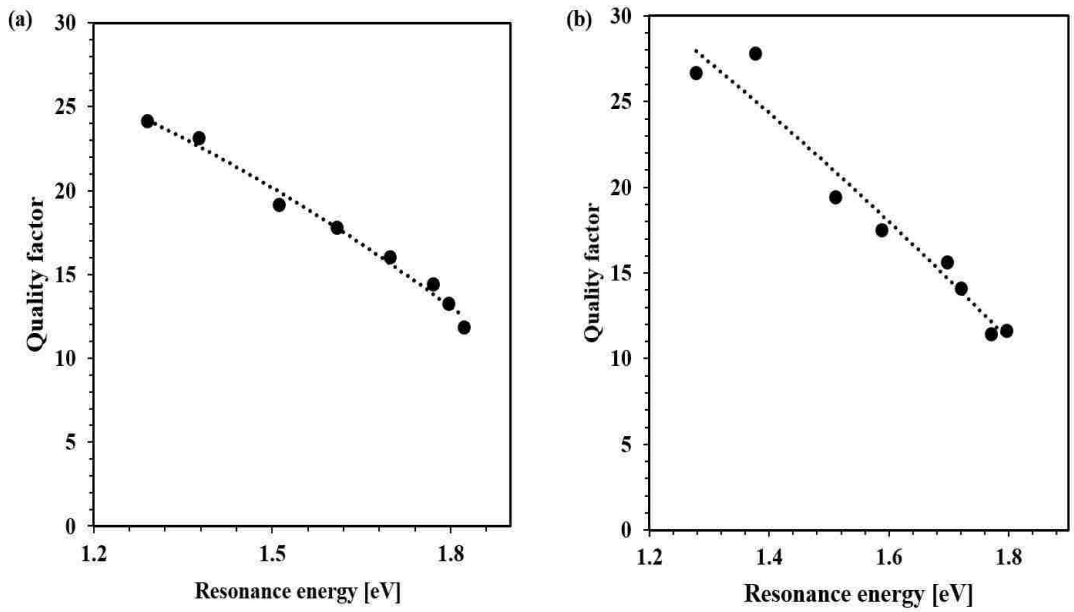

Figure 5.9: Quality factor $Q = E_{res}/\Gamma$ of single nanorods with various thickness as a function of resonance energy (a) absorption and (b) enhancement.

Figure 5.9 describes the quality factor which is defined as the enhancement of the oscillation amplitude of a driven oscillation system with respect to the driving amplitude [1],with different thicknesses of gold nanorods as a function of resonance energy for both absorption and enhancement. The Quality factor in our case is the local-field enhancement. Figure 5.9 (a) for absorption and Figure 5.9 (b) for enhancement. As the thickness and the resonance energy increase the amplitude of the quality factors decrease for both absorption and enhancement. Similar behavior is observed for both cases. Local field enhancement of the oscillation amplitude of a plasmonic system with respect to the driving amplitude is defined as the quality factor, $Q_f = E_{res}/\Gamma$ [1]. Figure 5.9 shows high quality factors around 24 for absorption and 27 for enhancement because of suppressed interband damping.

6 Chapter: DARK FIELD SPECTROSCOPY

6.1 Procedure

Samples were fabricated and images were taken by the SEM; then samples were used for dark field spectroscopy measurement. Figure 6.1 is a schematic diagram of the working principle of dark field spectroscopy. White light with a polarization is used to illuminate the sample, and then scattered light from the sample is collected by the 50x microscope objective (NA = 0.55, f = 200 nm) [78].

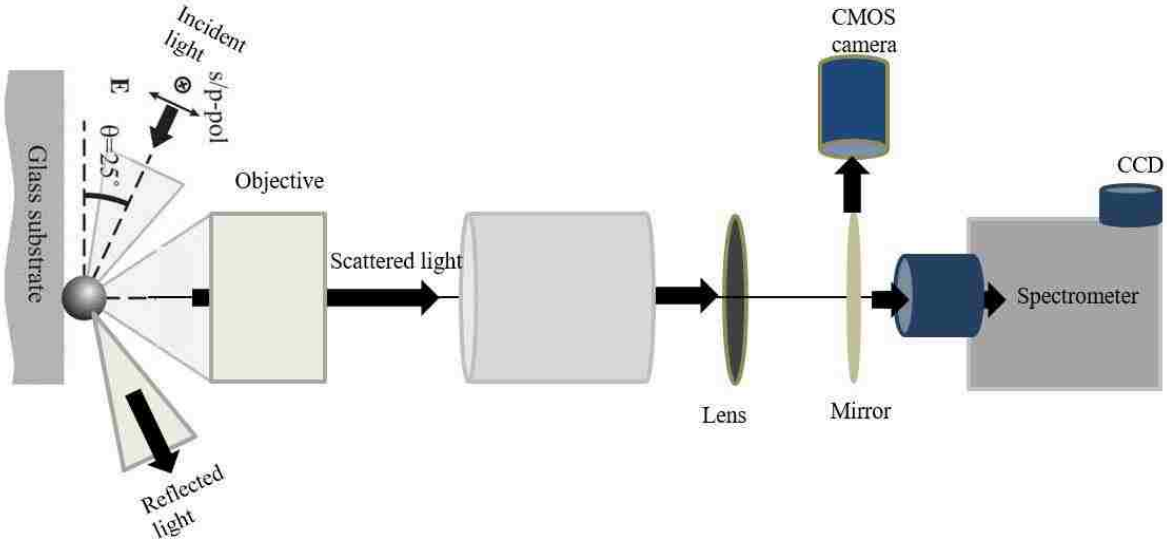

Figure 6.1: Working principle of the dark field spectroscopy

A flip-mounted mirror is used to direct the scattered light to the CMOS camera to take color images of the sample. To get the spectra, a Princeton Instrument Insight: 100B spectrometer system with a PIXIS 100B image sensor was used. Inside the spectrometer, a reflection grating with150 grooves/nm and a blaze angle of 800 nm was used, and the center wavelength was set at 750 nm. In this study, the CCD was exposed to the scattered light for 3500 ms.

6.2 Measurements

Preliminary experimental results are shown in Figure 6.2. Generally, it shows that the spectra from each nanorod are similar. There is small resonance peaks shifting for different nanorods but those are not significant. More work needs to be done optimizing the system to obtain more accurate result.

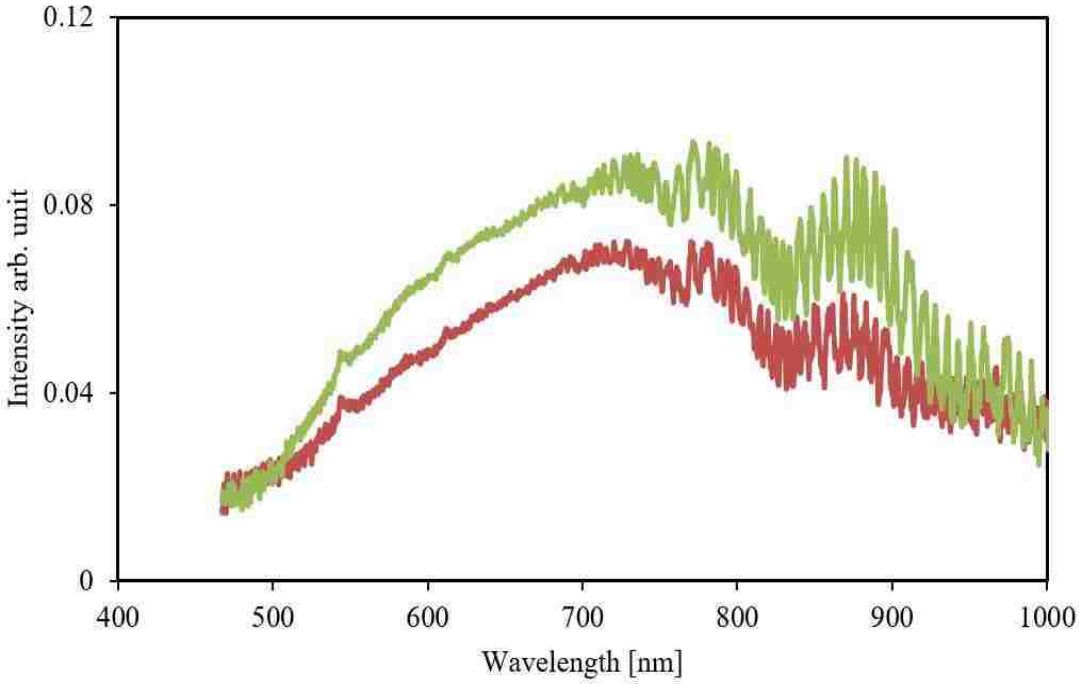

Figure 6.2: Measured scattering intensity of the gold nanorods.

7 Chapter: CONCLUSION

In this study, plasmonic properties of gold nanorods with various thicknesses were analyzed by finite element method. Sharp-corner and round-corner rectangular nanorods were studied. The length and width of the nanorods were kept constant and only thicknesses were varied thought the whole study. Many researchers have analyzed plasmonic properties of nanorods with different aspect ratio (ratio between major axis lengths over minor axis length), different substrates, different surrounding medium, chemically produced nanorods, electron beam lithography produced nanorods and different metals etc.

Plasmonic properties have strong dependence on the incident light polarization. For two different polarizations (longitudinal and transverse), absorption and enhancement spectra show significant difference in nature. Using two different incident light polarizations, absorption and enhancement spectra were studied. Resonance peaks of the spectra shifted toward blue for both absorption and enhancement spectra with increasing thicknesses of gold. For small thickness, the electrons confined and oscillate in a relatively larger space than larger thickness and as a result their peak resonance wavelength is larger. For higher thickness, the electrons confined and oscillate in a relative smaller space in corners of the nanorods as we see from the surface charge distributions plot. As a result their resonance frequency is relatively higher as well as their peak resonance wavelength lower than smaller thicknesses, which is very interesting because many people studied increasing length of the nanorods and they have found with increasing the length of the nanorod resonance peaks shifts towards red. For the same gold thickness, the peak resonance wavelength and normalized amplitude has a significant difference for both absorption and enhancement for both polarization. For polarization along the long axis, electrons oscillate in a larger space and as a result the peak resonance wavelength is longer than polarization along the

short axis of the nanorods. From the electric field distributions, it was found that with increasing the gold thicknesses the intensity decreases, because in larger thickness the electrons confined in corners as a result the electric field gets weaker inside the nanorods results lower absorption and enhancement. Surface charge distributions have shown in this work. From the distributions it is obvious that at the resonant wavelength the surface charge distributions show dipolar character while at other wavelengths it shows more quadrupole character.

In this study, Full width half maximum (FWHM) of the absorption and enhancement spectra were analyzed, and found strong dependence on the thicknesses of the gold nanorod. As the thickness increases, the FWHM of the spectrum also increases. The quality factor for the nanorods are higher that indicates it can show large local-field enhancement in the optical regime and making nanorods interesting for a range of optical application [1]. Sample was fabricated using electron beam lithography and preliminary data for the scattering spectra were taken by dark field spectroscopy.

8 REFERENCES

[1] C. Sönnichsen, T. Franzl, T. Wilk, G. von Plessen, J. Feldmann, O. Wilson, and P. Mulvaney, "Drastic Reduction of Plasmon Damping in Gold Nanorods," *Phys. Rev. Lett.*, vol. 88, no. 7, p. 77402, Jan. 2002.

[2] U. Kreibig and M. Vollmer, *Optical Properties of Metal Clusters*. Springer Science & Business Media, 2013.

[3] M. D. Wissert, C. Moosmann, K. S. Ilin, M. Siegel, U. Lemmer, and H.-J. Eisler, "Gold nanoantenna resonance diagnostics via transversal particle plasmon luminescence," *Opt. Express*, vol. 19, no. 4, p. 3686, Feb. 2011.

[4] "Fernandez-Garcia-R-2013-PhD-Thesis.pdf." .

[5] E. Massa, S. A. Maier, and V. Giannini, "An analytical approach to light scattering from small cubic and rectangular cuboidal nanoantennas," *New J. Phys.*, vol. 15, no. 6, p. 63013, Jun. 2013.

[6] H. Dai, M. Li, Y. Li, H. Yu, F. Bai, and X. Ren, "Effective light trapping enhancement by plasmonic Ag nanoparticles on silicon pyramid surface," *Opt. Express*, vol. 20, no. S4, p. A502, Jul. 2012.

[7] J. N. Farahani, D. W. Pohl, H.-J. Eisler, and B. Hecht, "Single Quantum Dot Coupled to a Scanning Optical Antenna: A Tunable Superemitter," *Phys. Rev. Lett.*, vol. 95, no. 1, p. 17402, Jun. 2005.

[8] P. J. Schuck, D. P. Fromm, A. Sundaramurthy, G. S. Kino, and W. E. Moerner, "Improving the Mismatch between Light and Nanoscale Objects with Gold Bowtie Nanoantennas," *Phys. Rev. Lett.*, vol. 94, no. 1, p. 17402, Jan. 2005.

[9] P. Mühlschlegel, H.-J. Eisler, O. J. F. Martin, B. Hecht, and D. W. Pohl, "Resonant optical antennas," *Science*, vol. 308, no. 5728, pp. 1607–1609, Jun. 2005.

[10] S. Zhang, K. Bao, N. J. Halas, H. Xu, and P. Nordlander, "Substrate-Induced Fano Resonances of a Plasmonic Nanocube: A Route to Increased-Sensitivity Localized Surface

Plasmon Resonance Sensors Revealed," *Nano Lett.*, vol. 11, no. 4, pp. 1657–1663, Apr. 2011.

[11] J. Ozhikandathil and M. Packirisamy, "Simulation and Implementation of a Morphology-Tuned Gold Nano-Islands Integrated Plasmonic Sensor," *Sensors*, vol. 14, no. 6, pp. 10497–10513, Jun. 2014.

[12] V. Giannini, A. Berrier, S. A. Maier, J. A. Sánchez-Gil, and J. G. Rivas, "Scattering efficiency and near field enhancement of active semiconductor plasmonic antennas at terahertz frequencies," *Opt. Express*, vol. 18, no. 3, pp. 2797–2807, Feb. 2010.

[13] H. A. Macpherson and C. R. Stoldt, "Iron pyrite nanocubes: size and shape considerations for photovoltaic application," *ACS Nano*, vol. 6, no. 10, pp. 8940–8949, Oct. 2012.

[14] D. Derkacs, S. H. Lim, P. Matheu, W. Mar, and E. T. Yu, "Improved performance of amorphous silicon solar cells via scattering from surface plasmon polaritons in nearby metallic nanoparticles," *Appl. Phys. Lett.*, vol. 89, no. 9, p. 93103, Aug. 2006.

[15] S. Mokkapati and K. R. Catchpole, "Nanophotonic light trapping in solar cells," *J. Appl. Phys.*, vol. 112, no. 10, p. 101101, Nov. 2012.

[16] X. Li, N. P. Hylton, V. Giannini, K.-H. Lee, N. J. Ekins-Daukes, and S. A. Maier, "Bridging electromagnetic and carrier transport calculations for three-dimensional modelling of plasmonic solar cells," *Opt. Express*, vol. 19 Suppl 4, pp. A888-896, Jul. 2011.

[17] K. R. Catchpole and A. Polman, "Plasmonic solar cells," *Opt. Express*, vol. 16, no. 26, p. 21793, Dec. 2008.

[18] V. E. Ferry, M. A. Verschuuren, H. B. T. Li, E. Verhagen, R. J. Walters, R. E. I. Schropp, H. A. Atwater, and A. Polman, "Light trapping in ultrathin plasmonic solar cells," *Opt. Express*, vol. 18, no. S2, p. A237, Jun. 2010.

[19] S. Pillai, K. R. Catchpole, T. Trupke, and M. A. Green, "Surface plasmon enhanced silicon solar cells," *J. Appl. Phys.*, vol. 101, no. 9, p. 93105, May 2007.

[20] C. Saylor, E. Novak, D. Debu, and J. B. Herzog, “Investigation of maximum optical enhancement in single gold nanowires and triple nanowire arrays,” *J. Nanophotonics*, vol. 9, no. 1, pp. 093053–093053, 2015.

[21] Y.-H. Qiu, F. Nan, Y.-F. Zhang, J.-H. Wang, G.-Y. He, L. Zhou, and Q.-Q. Wang, “Size-dependent plasmon relaxation dynamics and saturable absorption in gold nanorods,” *J. Phys. Appl. Phys.*, vol. 49, no. 18, p. 185107, 2016.

[22] P. K. Jain and M. A. El-Sayed, “Plasmonic coupling in noble metal nanostructures,” *Chem. Phys. Lett.*, vol. 487, no. 4–6, pp. 153–164, Mar. 2010.

[23] K. L. Kelly, E. Coronado, L. L. Zhao, and G. C. Schatz, “The Optical Properties of Metal Nanoparticles: The Influence of Size, Shape, and Dielectric Environment,” *J. Phys. Chem. B*, vol. 107, no. 3, pp. 668–677, Jan. 2003.

[24] E. Massa, S. A. Maier, and V. Giannini, “An analytical approach to light scattering from small cubic and rectangular cuboidal nanoantennas,” *New J. Phys.*, vol. 15, no. 6, p. 63013, Jun. 2013.

[25] F. Wang and Y. R. Shen, “General Properties of Local Plasmons in Metal Nanostructures,” *Phys. Rev. Lett.*, vol. 97, no. 20, p. 206806, Nov. 2006.

[26] L. Shao, Y. Tao, Q. Ruan, J. Wang, and H.-Q. Lin, “Comparison of the plasmonic performances between lithographically fabricated and chemically grown gold nanorods,” *Phys Chem Chem Phys*, vol. 17, no. 16, pp. 10861–10870, 2015.

[27] C. Langhammer, B. Kasemo, and I. Zorić, “Absorption and scattering of light by Pt, Pd, Ag, and Au nanodisks: Absolute cross sections and branching ratios,” *J. Chem. Phys.*, vol. 126, no. 19, p. 194702, 2007.

[28] M. W. Knight, L. Liu, Y. Wang, L. Brown, S. Mukherjee, N. S. King, H. O. Everitt, P. Nordlander, and N. J. Halas, “Aluminum Plasmonic Nanoantennas,” *Nano Lett.*, vol. 12, no. 11, pp. 6000–6004, Nov. 2012.

[29] M. W. Knight, N. S. King, L. Liu, H. O. Everitt, P. Nordlander, and N. J. Halas, “Aluminum for Plasmonics,” *ACS Nano*, vol. 8, no. 1, pp. 834–840, Jan. 2014.

[30] Y. Ekinci, H. H. Solak, and J. F. Löffler, “Plasmon resonances of aluminum nanoparticles and nanorods,” *J. Appl. Phys.*, vol. 104, no. 8, p. 83107, Oct. 2008.

[31] O. Lecarme, Q. Sun, K. Ueno, and H. Misawa, “Robust and Versatile Light Absorption at Near-Infrared Wavelengths by Plasmonic Aluminum Nanorods,” *ACS Photonics*, vol. 1, no. 6, pp. 538–546, Jun. 2014.

[32] R. Giannini, C. V. Hafner, and J. F. Löffler, “Scaling Behavior of Individual Nanoparticle Plasmon Resonances,” *J. Phys. Chem. C*, vol. 119, no. 11, pp. 6138–6147, Mar. 2015.

[33] O. L. Muskens, V. Giannini, J. A. Sánchez-Gil, and J. Gómez Rivas, “Optical scattering resonances of single and coupled dimer plasmonic nanoantennas,” *Opt. Express*, vol. 15, no. 26, p. 17736, 2007.

[34] Y. Huang and D.-H. Kim, “Dark-field microscopy studies of polarization-dependent plasmonic resonance of single gold nanorods: rainbow nanoparticles,” *Nanoscale*, vol. 3, no. 8, p. 3228, 2011.

[35] Y. Huang, X. Zhang, E. Ringe, M. Hou, L. Ma, and Z. Zhang, “Tunable Lattice Coupling of Multipole Plasmon Modes and Near-Field Enhancement in Closely Spaced Gold Nanorod Arrays,” *Sci. Rep.*, vol. 6, p. 23159, Mar. 2016.

[36] J. Zhu, “Shape dependent full width at half maximum of the absorption band in gold nanorods,” *Phys. Lett. A*, vol. 339, no. 6, pp. 466–471, May 2005.

[37] E. Stefan Kooij and B. Poelsema, “Shape and size effects in the optical properties of metallic nanorods,” *Phys. Chem. Chem. Phys. PCCP*, vol. 8, no. 28, pp. 3349–3357, Jul. 2006.

[38] P. K. Jain, K. S. Lee, I. H. El-Sayed, and M. A. El-Sayed, “Calculated Absorption and Scattering Properties of Gold Nanoparticles of Different Size, Shape, and Composition: Applications in Biological Imaging and Biomedicine,” *J. Phys. Chem. B*, vol. 110, no. 14, pp. 7238–7248, Apr. 2006.

[39] A. M. Hill, A. I. Nusir, P. V. Nguyen, O. M. Manasreh, and J. B. Herzog, "Computational electromagnetic analysis of plasmonic effects in interdigital photodetectors," 2014, vol. 9163, p. 91633Q–91633Q–5.

[40] G. P. Abbey, A. I. Nusir, O. Manasreh, and J. B. Herzog, "Structural characteristics of Au-GaAs nanostructures for increased plasmonic optical enhancement," 2016, p. 97580N.

[41] J. Wu, X. Lu, Q. Zhu, J. Zhao, Q. Shen, L. Zhan, and W. Ni, "Angle-Resolved Plasmonic Properties of Single Gold Nanorod Dimers," *Nano-Micro Lett.*, vol. 6, no. 4, pp. 372–380, Sep. 2014.

[42] J.-M. Jin, *Theory and Computation of Electromagnetic Fields*. John Wiley & Sons, 2011.

[43] "Computational Electromagnetics, Spring 2012." [Online]. Available: http://cs.nyu.edu/courses/spring12/CSCI-GA.2945-001/index.html. [Accessed: 26-Jun-2016].

[44] T. J. R. Hughes, L. P. Franca, and G. M. Hulbert, "A new finite element formulation for computational fluid dynamics: VIII. The galerkin/least-squares method for advective-diffusive equations," *Comput. Methods Appl. Mech. Eng.*, vol. 73, no. 2, pp. 173–189, May 1989.

[45] S. A. Maier, *Plasmonics: Fundamentals and Applications*. Springer Science & Business Media, 2007.

[46] D. J. Griffiths, *Introduction to Electrodynamics*, 4 edition. Boston: Pearson, 2012.

[47] R. W. Boyd, *Nonlinear Optics*. Academic Press, 2003.

[48] J. D. Jackson, *Classical Electrodynamics Third Edition*, 3 edition. New York: Wiley, 1998.

[49] S. J. Bauman, "Fabrication of Sub-10 nm Metallic Structures via Nanomasking Technique for Plasmonic Enhancement Applications," M.S., University of Arkansas, United States -- Arkansas, 2015.

[50] D. Sarid and W. Challener, *Modern Introduction to Surface Plasmons: Theory, Mathematica Modeling, and Applications*. Cambridge University Press, 2010.

[51] M. A. El-Sayed, "Small Is Different: Shape-, Size-, and Composition-Dependent Properties of Some Colloidal Semiconductor Nanocrystals," *Acc. Chem. Res.*, vol. 37, no. 5, pp. 326–333, May 2004.

[52] P. K. Jain, X. Huang, I. H. El-Sayed, and M. A. El-Sayed, "Noble Metals on the Nanoscale: Optical and Photothermal Properties and Some Applications in Imaging, Sensing, Biology, and Medicine," *Acc. Chem. Res.*, vol. 41, no. 12, pp. 1578–1586, Dec. 2008.

[53] K. Kolwas and A. Derkachova, "Damping rates of surface plasmons for particles of size from nano- to micrometers; reduction of the nonradiative decay," *J. Quant. Spectrosc. Radiat. Transf.*, vol. 114, pp. 45–55, Jan. 2013.

[54] K. L. Kelly, E. Coronado, L. L. Zhao, and G. C. Schatz, "The Optical Properties of Metal Nanoparticles: The Influence of Size, Shape, and Dielectric Environment," *J. Phys. Chem. B*, vol. 107, no. 3, pp. 668–677, Jan. 2003.

[55] P. K. Jain, S. Eustis, and M. A. El-Sayed, "Plasmon Coupling in Nanorod Assemblies: Optical Absorption, Discrete Dipole Approximation Simulation, and Exciton-Coupling Model," *J. Phys. Chem. B*, vol. 110, no. 37, pp. 18243–18253, Sep. 2006.

[56] M. Meier and A. Wokaun, "Enhanced fields on large metal particles: dynamic depolarization," *Opt. Lett.*, vol. 8, no. 11, p. 581, Nov. 1983.

[57] O. J. F. Martin and N. B. Piller, "Electromagnetic scattering in polarizable backgrounds," *Phys. Rev. E*, vol. 58, no. 3, pp. 3909–3915, Sep. 1998.

[58] A. D. Yaghjian, "Electric dyadic Green's functions in the source region," *Proc. IEEE*, vol. 68, no. 2, pp. 248–263, Feb. 1980.

[59] S. Enoch and N. Bonod, Eds., *Plasmonics*, vol. 167. Berlin, Heidelberg: Springer Berlin Heidelberg, 2012.

[60] W. Srituravanich, N. Fang, C. Sun, Q. Luo, and X. Zhang, “Plasmonic Nanolithography,” *Nano Lett.*, vol. 4, no. 6, pp. 1085–1088, Jun. 2004.

[61] E. Spiller, R. Feder, and J. Topallan, “SOFT X-RAYS FOR BIOLOGICAL AND INDUSTRIAL PATTERN REPLICATIONS,” *J. Phys. Colloq.*, vol. 39, no. C4, pp. C4-205-C4-211, Jul. 1978.

[62] P. D. L. Reimer, “Electron Optics of a Scanning Electron Microscope,” in *Scanning Electron Microscopy*, Springer Berlin Heidelberg, 1998, pp. 13–56.

[63] G. M. Wallraff and W. D. Hinsberg, “Lithographic Imaging Techniques for the Formation of Nanoscopic Features,” *Chem. Rev.*, vol. 99, no. 7, pp. 1801–1822, Jul. 1999.

[64] Z. W. A. Lateef, “Proton, Helium and Carbon Radiation Beam Targeting Reactive Oxygen, Nitrogen and Halogenated Species in TRIM-SRIM Model,” *J. Al-Nahrain Univ. - Sci.* □□ □□ □□ □□ □□□□□□- □□ □□□ □□□□□□ □□, vol. 15, no. 1, pp. 65–72, 2012.

[65] D. F. Kyser and N. S. Viswanathan, “Monte Carlo simulation of spatially distributed beams in electron-beam lithography,” *J. Vac. Sci. Technol.*, vol. 12, no. 6, pp. 1305–1308, Nov. 1975.

[66] M. URBÁNEK, V. KOLAŘÍK, S. KRÁTKÝ, M. MATĚJKA, M. HORÁČEK, and J. CHLUMSKÁ, “MONTE CARLO SIMULATION OF PROXIMITY EFFECT IN E-BEAM LITHOGRAPHY,” in *Proceedings of the 5th International conference NANOCON 2013*, pp. 723–726.

[67] J. B. Herzog, M. W. Knight, Y. Li, K. M. Evans, N. J. Halas, and D. Natelson, “Dark Plasmons in Hot Spot Generation and Polarization in Interelectrode Nanoscale Junctions,” *Nano Lett.*, vol. 13, no. 3, pp. 1359–1364, Mar. 2013.

[68] J. B. Herzog, M. W. Knight, and D. Natelson, “Thermoplasmonics: Quantifying Plasmonic Heating in Single Nanowires,” *Nano Lett.*, vol. 14, no. 2, pp. 499–503, Feb. 2014.

[69] T. C. Choy, *Effective Medium Theory: Principles and Applications*. Oxford University Press, 2015.

[70] P. B. Johnson and R. W. Christy, “Optical Constants of the Noble Metals,” *Phys. Rev. B*, vol. 6, no. 12, pp. 4370–4379, Dec. 1972.

[71] “Using Perfectly Matched Layers and Scattering Boundary Conditions for Wave Electromagnetics Problems,” *COMSOL Blog*, 28-Jan-2015. .

[72] P. YU and M. Cardona, *Fundamentals of Semiconductors: Physics and Materials Properties*. Springer Science & Business Media, 2005.

[73] J. Solé, L. Bausa, and D. Jaque, *An Introduction to the Optical Spectroscopy of Inorganic Solids*. John Wiley and Sons, 2005.

[74] N. D. Spencer and J. H. Moore, *Encyclopedia of Chemical Physics and Physical Chemistry: Fundamentals*. Taylor & Francis, 2001.

[75] E. Hecht, *Optics*. Addison-Wesley, 2002.

[76] “Refractive index of Au (Gold) - Johnson.” [Online]. Available: http://refractiveindex.info/?shelf=main&book=Au&page=Johnson. [Accessed: 19-Jun-2016].

[77] M. Song, G. Chen, Y. Liu, E. Wu, B. wu, and H. Zeng, “Polarization properties of surface plasmon enhanced photoluminescence from a single Ag nanowire,” *Opt. Express*, vol. 20, no. 20, p. 22290, Sep. 2012.

[78] D. A. French, S. J. Bauman, A. Darweesh, D. Debu, P. K. Ghosh, and J. B. Herzog, “Plasmonic resonance shift for various nanodevice geometries,” 2016, vol. 9836, p. 98362X–98362X–6.